

## ABSTRACT

Estimation & optimization (& hence reduction) of base drag on a subsonic missile using CFD analysis for different base configuration. The missile is studied (analyzed) for different base configuration at different angle of attacks using ANSYS. The missile is modeled and meshed using ICEM CFD and analyzed for different velocities and angle of attack using FLUENT. This study is done on 3 different base configurations and the base producing the least base drag is found out.

Base drag, arising from flow separation at the blunt base of a body can be a sizeable fraction of total drag in the context of projectiles, missiles and after bodies of fighter aircrafts. The Base drag is the major contribution of total drag for low speed regimes, flight tests have shown that the base drag may account for up to 50% of the total drag. An Experimental investigation for simple hemispherical flight vehicle body of length 500mm and diameter 50mm was conducted for the purpose of investigating the base drag. The base drags for three configurations are calculated and the results are compared with the CFD data. The three configurations used are

- (i) Flat Base configuration,
- (ii) Closed Nozzle configuration and
- (iii) Boat Tail Configuration.

The evaluation of base drag for three different flow velocities such as

(i) 20 m/s, (ii) 35 m/s and (iii) 50 m/s at three different angle of attack such as -2, 0 and 2 degree AOA are and compared.

# TABLE OF CONTENTS

## CHAPTERS

1.	INTRODUCTION .....	1
	BASE DRAG .....	1
	FACTORS AFFECTING BASE DRAG.....	1
	BOAT TAIL CONFIGURATION.....	2
	FACTORS AFFECTRING BOAT TAIL DRAG .....	2
	NOZZLE BASE DRAG.....	3
	FACTORS AFFECTING NOZZLE BASE DRAG .....	3
	CYLINDER AERODYNAMICS.....	3
	MISSILE GEOMETRIES TO BE INVESTIGATED...	5
2.	LITERATURE REVIEW.....	6
3.	SOLVER DETAILS .....	10
	ANSYS ICEM CFD.....	10
	HiFUN .....	11
4.	METHODOLOGY .....	
	MESHES .....	12
	DENSITY BASED SOLVER .....	13
	BOUNDARY CONDITIONS USED .....	15
	FLOW CONDITIONS .....	16
5.	RESULTS AND DISCUSSION .....	
	Cp DISTRIBUTION OVER THE SURFACE OF THE MISSILE	
	BODY .....	17
	ESTIMATED DRAG VALUES.....	37
	Cd PLOTS FOR DIFFERENT AOA .....	38
	VELOCITY CONTOUR.....	44
6.	CONCLUSION .....	48
7.	REFERENCES .....	49

## List of Figures

Fig 1.1 Base Line Configuration

Fig 1.2 Boat Tail

Fig 1.3 Nozzle Base

Fig 1.4.1 Drag for a blunt body

Fig 1.4.2 Flow patterns for circular cylinder normal to the flow for different Reynolds Number

Fig 1.5.1 Baseline Configuration

Fig 1.5.2 Boat tail Configuration

Fig 1.5.3 Nozzle Configuration

Fig 4.1.1. Flatbase configuration

Fig 4.1.2 Boat tail Configuration

Fig 4.1.3. Nozzle base Configuration

Figure 4.3 Overview of the Pressure-Based Solution Methods

Fig 5.1.1. Cp distribution on flat base

Fig 5.1.2. Cp Distribution on the boat tail base

Fig 5.1.3. Cp distribution on nozzle base

Fig 5.1.4. Cp along the base of flat base at 0 AoA (20m/s)

Fig 5.1.5. Cp along flatbase at 2 AoA (20 m/s)

Fig 5.1.6. Cp along flatbase at -2 AoA (20m/s)

Fig 5.1.7. Comparison of Cp of flatbase for different AoA at 20 m/s

Fig 5.1.8. Cp along boattail at 0 AoA (20 m/s)

Fig 5.1.9. Cp along boattail at 2 AoA (20 m/s)

Fig 5.1.10. Cp along boattail at -2 AoA (20 m/s)

Fig 5.1.11. Comparison of Cp of boattail base for different AoA at 20 m/s

Fig 5.1.12. Cp along nozzle base at 0 AoA (20 m/s)

Fig 5.1.13.  $C_p$  along nozzle base at 2 AoA (20 m/s)

Fig 5.1.14.  $C_p$  along nozzle base at -2 AoA (20 m/s)

Fig 5.1.15. Comparison of  $C_p$  of nozzle base for different AoA at 20 m/s

Fig 5.1.16.  $C_p$  along flatbase at 0 AoA (35 m/s)

Fig 5.1.17.  $C_p$  along flat base at 2 AoA (35 m/s)

Fig 5.1.18.  $C_p$  along flat base at -2 AoA (35 m/s)

Fig 5.1.19. Comparison of  $C_p$  of flat base for different AoA at 35 m/s

Fig 5.1.20.  $C_p$  along boat tail base at 0 AoA (35 m/s)

Fig 5.1.21.  $C_p$  along flat base at 2 AoA (35 m/s)

Fig 5.1.22.  $C_p$  along flat base at -2 AoA (35 m/s)

Fig 5.1.23. Comparison of  $C_p$  of boat tail base for different AoA at 35 m/s

Fig 5.1.24.  $C_p$  along nozzle base at 0 AoA (35 m/s)

Fig 5.1.25.  $C_p$  along nozzle base at 2 AoA (35 m/s)

Fig 5.1.26.  $C_p$  along nozzle base at -2 AoA (35 m/s)

Fig 5.1.27. Comparison of  $C_p$  of nozzle tail base for different AoA at 35 m/s

Fig 5.1.28.  $C_p$  along flat base at 0 AoA (50 m/s)

Fig 5.1.29.  $C_p$  along flat base at 2 AoA (50 m/s)

Fig 5.1.30.  $C_p$  along flat base at -2 AoA (50 m/s)

Fig 5.1.31. Comparison of  $C_p$  of flat tail base for different AoA at 50 m/s

Fig 5.1.32.  $C_p$  along boat tail base at 0 AoA (50 m/s)

Fig 5.1.33.  $C_p$  along boat tail base at 2 AoA (50 m/s)

Fig 5.1.34.  $C_p$  along boat tail base at -2 AoA (50 m/s)

Fig 5.1.35. Comparison of  $C_p$  of boat tail base for different AoA at 50 m/s

Fig 5.1.36.  $C_p$  along nozzle base at 0 AoA (50 m/s)

Fig 5.1.37.  $C_p$  along nozzle base at 2 AoA (50 m/s)

Fig 5.1.38.  $C_p$  along Nozzle base at -2 AoA (50 m/s)

Fig 5.1.39. Comparison of  $C_p$  of Nozzle base for different AoA at 50 m/s

Fig 5.3.1 Cd of flat base for different AoA at 20 m/s

Fig 5.3.2 Cd of Boat tail base for different AoA at 20 m/s

Fig 5.3.3 Cd of nozzle base for different AoA at 20 m/s

Fig 5.3.4. Comparison of Cd vs AoA for different configuration for 20 m/s

Fig 5.3.5 Cd of flat base for different AoA at 35 m/s

Fig 5.3.6. Cd of boat tail base for different AoA at 35 m/s

Fig 5.3.7 Cd of nozzle base for different AoA at 35 m/s

Fig 5.3.8. Comparison of Cd vs AoA for different configuration for 35 m/s

Fig 5.3.9. Cd of flat base for different AoA at 50 m/s

Fig 5.3.10. Cd of boat tail base for different AoA at 50 m/s

Fig 5.3.11 Cd of nozzle base for different AoA at 50 m/s

Fig 5.3.12. Comparison of Cd vs AoA for different configuration for 50 m/s

Fig 5.4.1. Velocity counter for flat base configuration at 20m/s and 0deg AOA

Fig 5.4.2 Velocity counter for flat base configuration at 50m/s and 0deg AOA

Fig 5.4.3. Velocity counter for boat tail base configuration at 35m/s and 0deg AOA

Fig 5.4.4. Velocity counter for boat tail base configuration at 50m/s and 0deg AOA

Fig 5.4.5. Velocity counter for nozzle base configuration at 20m/s and 0deg AOA

Fig 5.4.6. Velocity counter for nozzle base configuration at 35m/s and 0deg AOA

Fig 5.4.7. Velocity counter for nozzle base configuration at 50m/s and 0deg AOA

## List of Tables

Table 4.5 Boundary conditions used for different part of geometry.....	15
Table 4.6 Flow conditions.....	16

# **CHAPER 1**

## **INTRODUCTION**

The geometry of a cross section of a body strongly affects flow separation, reattachment point and vortex structure especially in subsonic and transonic regimes. As the edges become rounded off, the transition from turbulent to laminar flow separation occurs with the angle of incidence. The present study describes a computational analysis method to predict the aerodynamic characteristics of three geometry having circular cross sections: a hemispherical body with flat base, a flight body with a nozzle at the base and with boat tail configuration.

### **1.1. BASE DRAG**

One of the most important aerodynamic performance characteristics for flight vehicles is the total drag. The total drag for flight vehicles can be divided into three components: (i) pressure drag (excluding the base), (ii) viscous (skin friction) drag and (iii) base drag. The base drag is a major contributor to the total drag. Base drag is a component of aerodynamic drag caused by a partial vacuum in the flight vehicle's tail area. The vacuum is the hole created by the vehicle's passage through the air. Base drag changes during flight. While the motor is firing, the drag is minimal since the tremendous volume of gas generated by the motor fills this void. The drag takes a sharp jump at burnout when this gas disappears. The determination and minimization of base drag is done.

#### **1.1.1 Factors affecting Base Drag**

Base Drag is influenced by a variety of flow and geometrical parameters. With turbulent boundary layer ahead of the base, and in the absence of jet flow, the major factors include:

- (i) Mach number in free stream, just ahead of the base
- (ii) Boundary layer momentum thickness ahead of the base
- (iii) Base diameter
- (iv) Angle of attack
- (v) After body shape (boat-tail or flair angle, fore-body diameter, after-body length) and
- (vi) Parameters characterizing the base drag reduction device.

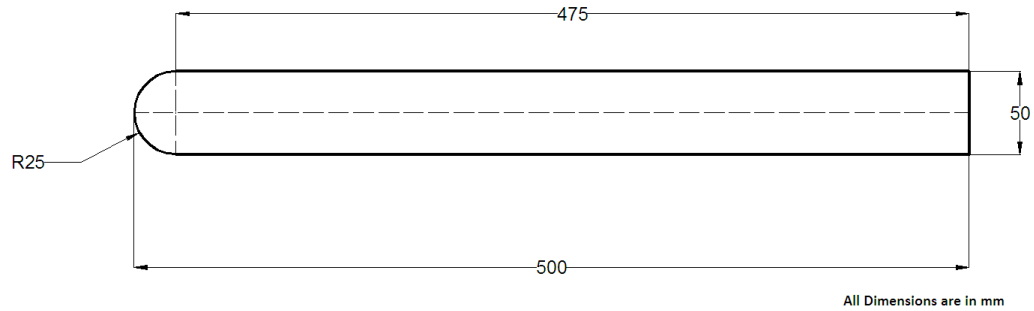


Fig 1.1 Base Line Configuration

## 1.2 BOAT TAIL DRAG

The conical section of a ballistic body that progressively decreases in diameter towards the tail to reduce overall aerodynamic drag is referred to as boat tail body and the drag so produced by this body is known as boat tail drag. Boat tail is the minimal drag when compared with that of base drag and nozzle shroud configuration drag.

### 1.2.1 Factors affecting Boat-Tail drag

- (i) Wind
- (ii) Vertical angles
- (iii) Ambient air density
- (iv) Magnus effect
- (v) Gyroscopic drift and Poisson effect.

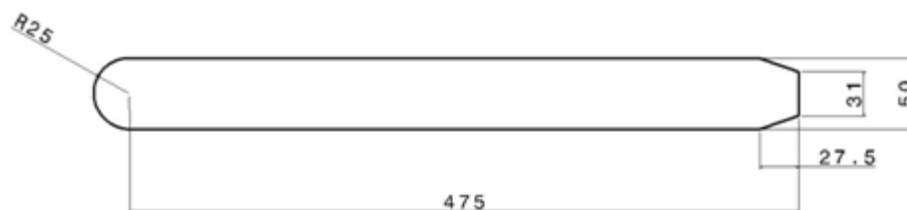


Fig 1.2 Boat Tail



## 1.3 Nozzle Base Drag

A nozzle shroud includes a centre body that is at least partially surrounded by an outer shroud. The outer shroud is readily spaced from the centre body to define a Pre-mixed flow passage there between the outer shroud includes a main body that defines an inner side portion ,an outer side portion and a forward end portion that is axially separated from and aft end portion.

### 1.3.1 Factors Affecting Nozzle Base Drag

- (i) Wind
- (ii) Vertical angles
- (iii) Ambient air density
- (iv) Boundary layer momentum thickness ahead of base
- (v) Base diameter



All Dimensions are in mm

Fig 1.3 Nozzle Base

## 1.4. CYLINDER AERODYNAMICS

At low-speed subsonic flow over a sphere or an infinite cylinder with its axis normal to the flow, if the flow were inviscid (frictionless) the streamlines would form a symmetric pattern; hence, the pressure distributions over the front and rear surfaces would also be symmetric. This symmetry creates a momentous phenomenon, namely, that there is no pressure drag on the sphere if the flow is frictionless. The actual flow over a sphere or cylinder, in the presence of friction leads to separated flows in regions of adverse pressure gradients. There will be separated flow on the back face of the cylinder, with a relatively

fat wake and with the associated high pressure drag; this case is sketched in the figure 4. The bar to the right of the figure denotes the total drag of the cylinder, the shaded portion of bar represents skin friction drag and the open portion represents the pressure drag. For the case of a blunt body the drag is relatively large and most of the drag is due to pressure drag.

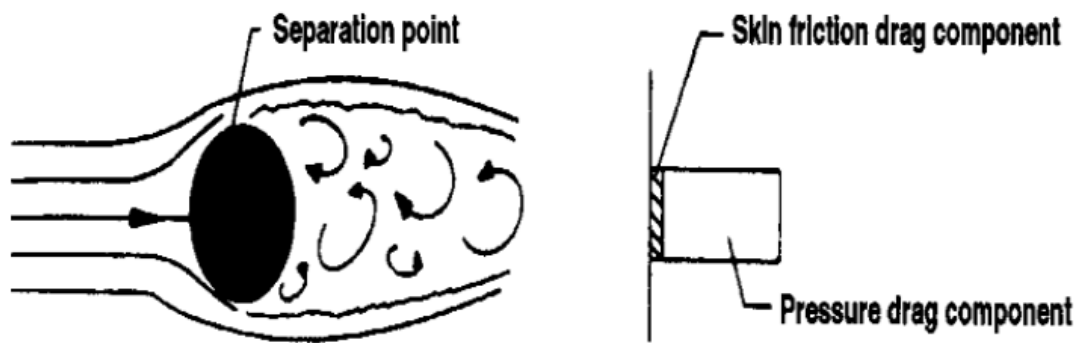


Fig 1.4 Drag for a blunt body

In the case of a circular cylinder the vortex shedding is most easily observed below the critical Reynolds number when the separation points are on the windward side of the cylinder. Above the critical Reynolds number the separation points move rearwards (leading to a narrower wake) and it has been reported that the vortex street gives way to a more-or-less random turbulent wake. The more recent work of Roshko and others has now demonstrated the persistence of periodic effects at Reynolds numbers well above the critical. In the light of this it seems clear that vortex shedding is a feature of the flow past circular cylinders throughout the Reynolds number range but that the vortices were not detected in the earlier investigations because they are more difficult to see.

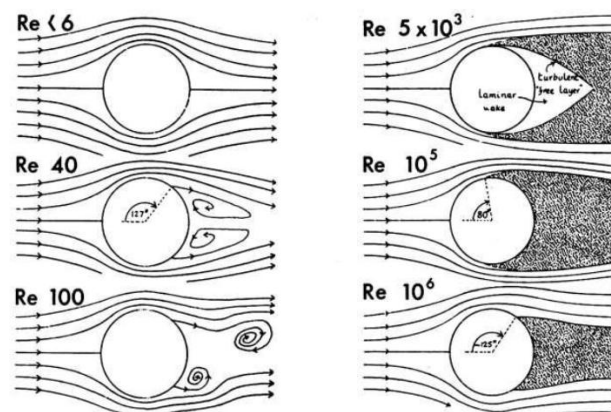


Fig 1.4.1 Flow patterns for circular cylinder normal to the flow for different Reynolds Number

## 1.5. MISSILE GEOMETRIES TO BE INVESTIGATED

The three missile geometries to be investigated for base drag are designed using the software CATIA V20 as shown in the following figures. All the three models considered are simple hemispherical bodies of length 500mm and cross sectional diameter 50mm.

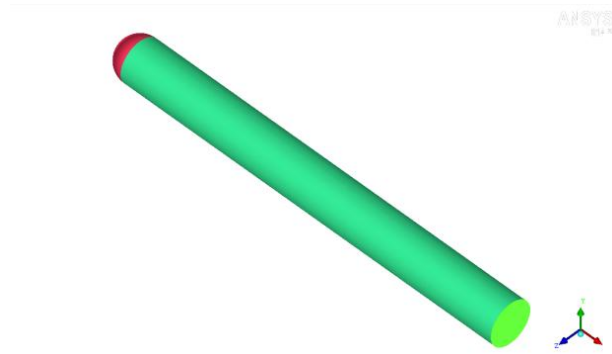


Fig 1.5.1 Baseline Configuration

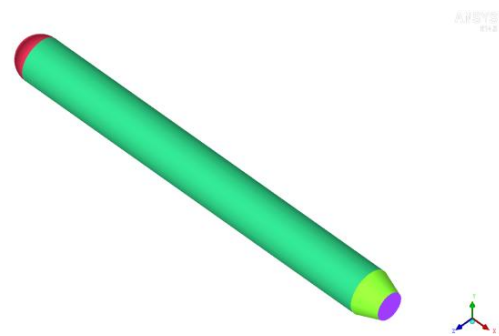


Fig 1.5.2 Boat tail Configuration

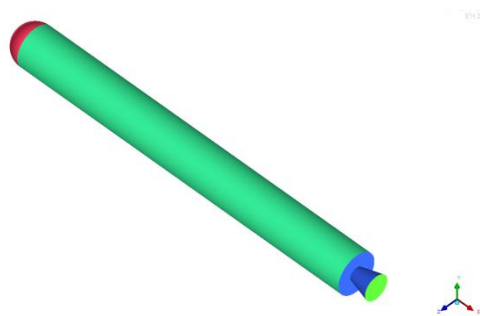


Fig 1.5.3 Nozzle Configuration

## **CHAPTER 2**

### **LITERATURE REVIEW**

#### **1. Aerodynamic configuration design of missile, P. Sethunathan**

From this paper the aerodynamic characteristics of various sections such as body, wing and tail of anti-aircraft missile were computed using analytical methods. Drag characterization is carried out at different Mach number at subsonic speed. To predict the normal force coefficient values linear wing theory, Newtonian impact theory and slender wing theory is used. Normal force coefficient were calculated at different AOA.

#### **2. The effect of various boat tail shapes on base pressure, B G Karpov**

The total drag decreases monotonically for boat tails longer than 0.5 calibers. For shorter boat tail, the drag is higher than that of a square based body. For boat tail length between 0.5-1.5 calibers, conical boat tail have lower drag than either the ogival or concave configuration. The base pressure decreases with boat tail length but increases with boat tail angle at the base.

#### **3. Aerodynamic analysis of a missile configuration using ANSYS-CFX,**

Hong Chuan Wee

The study used CFD code, ANSYS-CFX to predict the static aerodynamic characteristic of a missile configuration. The study was conducted for different mach number and the results were compared against experimental data from actual wind tunnel tests.

#### **4. CFD applications and validations in aerodynamic design and analysis for missiles, KwangSeop Lee, Seungkyu Hong**

CFD examples at Agency for defense development (ADD) are introduced to show their variety at its application in the course of a missile design. Boat tail and side jet interactions being one of the example for supersonic flow region. Various means of validation for those complex flows are also described.

#### **5. AGARD, General Missile aerodynamics, George G Brebner**

The difference in design objectives and therefore in geometric proportions of a missile mean that different aerodynamic calculation method may often be required for the applications. The six component of aerodynamic force and moment acting on a missile

are taken in turn, their importance discussed and their various characteristics describe, along with some comments on methods of estimating them.

## **6. (Mitchell.et.al, Study of the Base Pressure Distribution of a Slender Body of Square Cross-Section)**

A low-speed wind-tunnel investigation of a slender body of square cross-section was conducted to determine the effect of boat tail geometry on the base pressure coefficient. The data were obtained over an angle-of-attack range of 0 to 8 degrees. Munitions with square or rectangular cross-section have better volumetric efficiency than conventional munitions of circular section; such configurations have been the subject of continued interest. Most of the existing literature is concerned with the aerodynamics of such shapes which are complicated by the lack of axial symmetry. One aspect that had not been well investigated is the after body shape for minimum base drag. This paper reports an exploratory study of the base pressure coefficient of a body with a square cross-section. The experimental study is complemented by numerical modeling.

The test article comprised of five major components. The overall length of the model was 783.7 mm (30.853 in.). The nose cone was manufactured from acetyl copolymer, which was selected for its ease of machining. The rest of the model was constructed of 6061-T6 aluminum. The model was mounted such that the sides were horizontal and vertical.

## **7. (Hitchcock.al, ON ESTIMATING THE DRAG COEFFICIENT OF MISSILES)**

A method of estimating the head, base and friction drag coefficient of a missile is outlined. This procedure pertains to rockets and artillery projectiles, with or without fins, and is a combination of theory and empirical data, gathered from numerous sources.

Chapman showed that his theory could be applied to boat tailed bodies providing the boundary layer on the boat tail is laminar, but not if it is turbulent. The drag coefficient is a function of  $M$ . The ratio of the drag coefficient of a missile to that of a typical projectile is called its form factor relative to the typical projectile, where  $f$  represents the type of projectile. If there is a typical projectile on which is nearly constant its, tabulated drag coefficient multiplied by the average  $f$  may be used as the estimated drag coefficient of the missile.

## **8. (Frank G) IMPROVED EMPIRICAL MODEL FOR BASE DRAG PREDICTION ON MISSILE CONFIGURATIONS BASED ON NEW WIND TUNNEL DATA**

New wind tunnel data have been taken, and a new empirical model has been developed for predicting base drag on missile configurations. The new wind tunnel data were taken at NASA/LaRC in the Unitary Plan Wind Tunnel at Mach numbers from 2.0 to 4.5, angles of attack to  $16^\circ$ , fin control deflections up to  $200^\circ$ , fin thickness to chord ( $t/c$ ) ratio of 0.05 to 0.15, and fin locations flush with the base to two chord lengths upstream of the base. The newly developed empirical model uses these data along with previous wind tunnel data. It estimates base drag as a function of all the above variables along with boat tail and power-on or power-off effects. In comparing the new empirical model to that used in the former aero-prediction code, the new model gives improved accuracy compared to wind tunnel data. The pressures on the model were measured with two electronically scanned pressure modules that were located inside the model. The modules had a full-scale range of  $\pm 5$  psi. All 89 pressure orifices on the model base were measured simultaneously for each data point. The model angle of attack was measured with an accelerometer that was mounted inside the missile body. The missile base drag coefficient was calculated using an area weighted average of the base pressure coefficients. As already discussed, when there is a tail located in the vicinity of the base, the base pressure is affected due to several parameters. IAP results for  $C_{p5}$  as a function of  $\delta$  compared to the results of the present test data of Wilcox. Also shown are the OAP results, which are straight lines because the OAP empirical model does not include  $\delta$  as one of its parameters, for  $t/c=0.05$  and  $e$  for  $t/c=0.10$ , and  $f$  for  $t/c=0.15$ . All are for  $x/ca=0$  and  $w$  given for several Mach numbers.

## **9. (W.A.Mair.et.al) Reduction of Base Drag by Boat- Tailed After bodies in Low speed flow**

A substantial reduction of drag has been obtained with an after body consisting of a smooth fairing leading to a conical tail piece of semi angle  $22^\circ$ . At the Reynolds number of these experiments this afterbody, with a length of only 60 percent of the maximum diameter, gave almost as much reduction of drag as a conventional streamline tail. Changes of boundary-layer thickness had only small effects on the drag reductions obtained with the boat tailed afterbodies. So that variations of Reynolds numbers might also be expected to have only small effects. At higher Reynolds number the drag

reduction obtained with conventional tail might be greater and such a tail might then compare rather more favorably with the boat –tailed afterbodies.

#### **10. (V.Menezes et.al.) Drag Reduction by Controlled Base Flow Separation**

The problems of wake flow at high speeds and the drag associated with it are a significant source of observation in the design of missiles, projectiles and other typical high speed vehicles. A large wake at the base of the vehicle would cause an increase in the overall drag due to the reduced base pressure. The wake studies of high speed bodies also gain importance due to the severe aerodynamic heating problem and high rise in the temperature of the base flow .Many methods were devised to reduce the base drag of such high speed bodies. These included boat-tailing, base bleed, base combustion, locked vortex afterbodies, ventilated cavities etc. Among these methods the boat tailed or conical after body concept was very popular and was found very effective in reducing base drag. All the base drag reduction studies carried out so far were on bodies in subsonic, transonic, supersonic flows. It was believed until recently that the wake flows of the body flying at hypersonic mach numbers were not so critical.

#### **11. (Sidra.ISilton.et.al) Base Drag Considerations on a 0.50 caliber spinning projectile.**

During the course of using computational fluid dynamics to determine the complete set of aerodynamic coefficients over the flight Machnumbers, the computed base pressure in the subsonic and transonic flight regimes were found to be quite large such that either a very small or negative base drag was observed. The present study investigates the cause of this phenomenon by investigating the flow in subsonic and transonic regimes at zero angle of attack. Additionally, the effect of boat tail and base geometry on the base drag was investigated in order to better understand the flow phenomenon leading to reduced base drag

# **CHAPTER 3**

## **SOLVER DETAILS**

### **3.1. ANSYS ICEM CFD**

ANSYS ICEM CFD offers mesh generation with the capacity to compute meshes with various different structures depending on the users requirements. It is a powerful and highly manipulative software which allows the user to generate grids of high resolution. This is a requirement as mesh generation is an inherently geometry dependent problem meaning there is no singular meshing method which can be used for every problem. ICEM CFD allows the following different types of grid structures to be created:

- Multi-block structured meshes
- Unstructured meshes
- Hybrid meshes

ICEM CFD provides a user interface which includes several components to make mesh generation intuitive and easy to use once its full capabilities are understood. The user interface contains a complete environment to create, modify and manage computational grids:

- Main Menu: Create/Open/Save/Close projects, Geometry/Mesh/Blocking options and parameters, Import/Export Model/Geometry/Mesh
- Utilities for visualization purposes: View/Zoom/Refresh screen, Undo/Redo commands, Wireframe/Solid Simple Display
- A hierarchical Display Control Tree: Model, Geometry/Mesh/Blocking/Parts
- Function Tabs to modify the mesh: Geometry/Mesh/Blocking, Edit Mesh, Properties/Constraints/Loads/FEA solver options, Output Mesh
- Selection Toolbar
- Data Entry Zone
- Message Window
- Histogram Window



### **3.2.HiFUN: High Resolution Flow Solver on Unstructured meshes**

The code HiFUN the primary product of Sandi, is a general purpose flow solver employing unstructured data based algorithms. Developed in the Department of Aerospace Engineering, Indian Institute of Science, the code is fine tuned to solve typical Aerospace applications and can be easily extended to solve certain flow problems encountered in automotive industries also. The code has been extensively used for solving a number of problems, over a wide range of Mach numbers, ranging from Airship aerodynamics to aerodynamics of hypersonic vehicles.

#### **Unstructured face based data allowing for arbitrary polyhedral volumes**

The solver allows the use of four basic mesh elements, namely, hexahedron, tetrahedron, prism and pyramid, in combination. The adaptive capability of the solver, allowing for hanging nodes, results in arbitrary polyhedral volumes.

- Higher order spatial accuracy
- Numerical flux formula
- Viscous discretization
- Non conformal block interface algorithm
- Moving wall boundary condition
- Multiple rotating frames of reference algorithm
- Algorithm to simulate porous media
- Turbulence models
- Wall function
- Convergence acceleration
- Parallel
- Higher order time accuracy
- Grid adaptation
- Migratory Memory Algorithm

# CHAPTER 4

## METHODOLOGY

### 4.1.Meshes

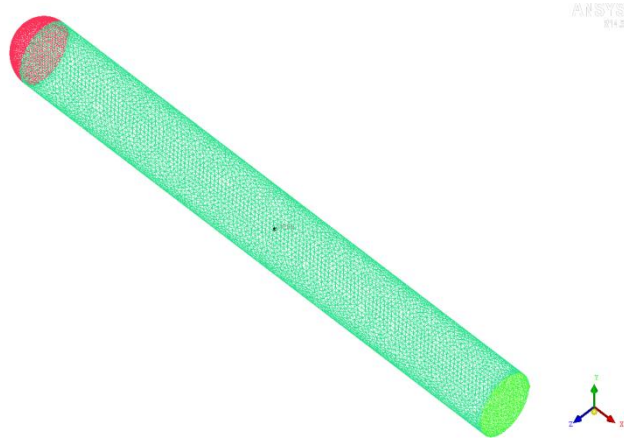


Fig 4.1.1.Flatbase configuration

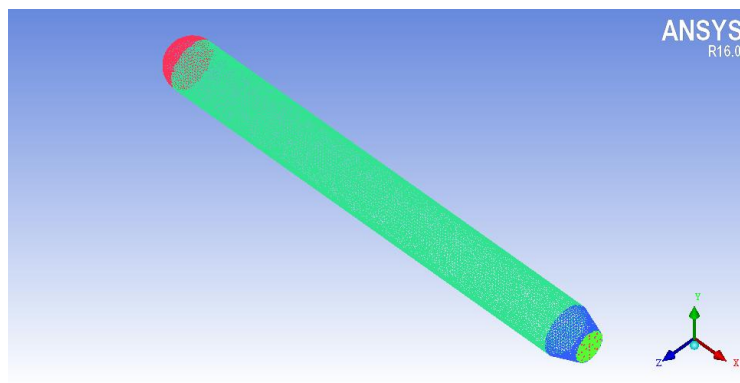


Fig 4.1.2 Boat tail Configuration

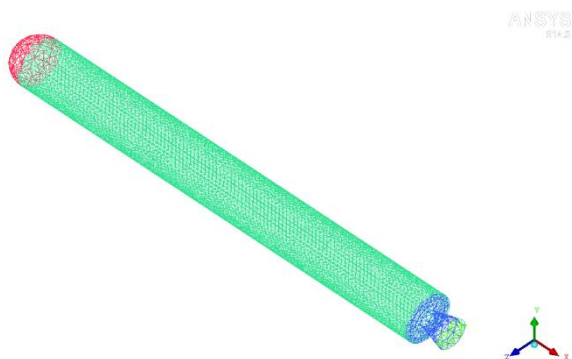


Fig 4.1.3.Nozzle base Configuration

## 4.2. Density-Based Solver

The density-based solver solves the governing equations of continuity, momentum, and (where appropriate) energy and species transport simultaneously (i.e., coupled together). Governing equations for additional scalars will be solved afterward and sequentially (i.e., segregated from one another and from the coupled set) using the procedure described in Section 4.2. Because the governing equations are non-linear (and coupled), several iterations of the solution loop must be performed before a converged solution is obtained. Each iteration consists of the steps illustrated in Figure 4.2.

1. Update the fluid properties based on the current solution. (If the calculation has just begun, the fluid properties will be updated based on the initialized solution.)
2. Solve the continuity, momentum, and (where appropriate) energy and species equations simultaneously.
3. Where appropriate, solve equations for scalars such as turbulence and radiation using the previously updated values of the other variables.
4. When interphase coupling is to be included, update the source terms in the appropriate continuous phase equations with a discrete phase trajectory calculation.
5. Check for convergence of the equation set.

These steps are continued until the convergence criteria are met.

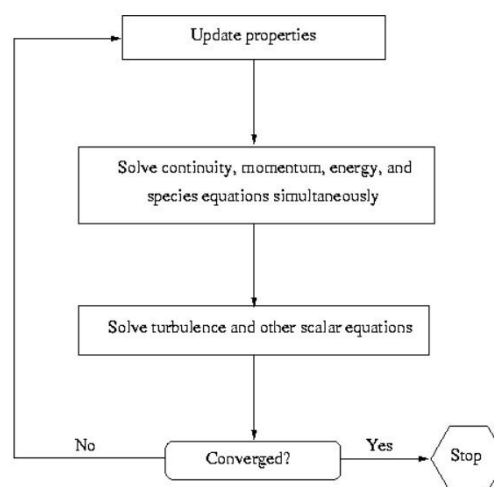


Fig 4.2 Density- based solver

In the density-based solution method, you can solve the coupled system of equations (continuity, momentum, energy and species equations if available) using, either the coupled-explicit formulation or the coupled-implicit formulation. The main distinction between the density-based explicit and implicit formulations is described next.

In the density-based solution methods, the discrete, non-linear governing equations are linearized to produce a system of equations for the dependent variables in every computational cell. The resultant linear system is then solved to yield an updated flow-field solution.

The manner in which the governing equations are linearized may take an "implicit" or "explicit" form with respect to the dependent variable (or set of variables) of interest. By implicit or explicit we mean the following:

Implicit: For a given variable, the unknown value in each cell is computed using a relation that includes both existing and unknown values from neighboring cells. Therefore each unknown will appear in more than one equation in the system, and these equations must be solved simultaneously to give the unknown quantities.

Explicit: For a given variable, the unknown value in each cell is computed using a relation that includes only existing values. Therefore each unknown will appear in only one equation in the system and the equations for the unknown value in each cell can be solved one at a time to give the unknown quantities.

In the density-based solution method you have a choice of using either an implicit or explicit linearization of the governing equations. This choice applies only to the coupled set of governing equations. Transport equations for additional scalars are solved segregated from the coupled set (such as turbulence, radiation, etc.). Regardless of whether you choose the implicit or explicit methods, the solution procedure shown in Figure 4.3.

If you choose the implicit option of the density-based solver, each equation in the coupled set of governing equations is linearized implicitly with respect to all dependent variables in the set. This will result in a system of linear equations with  $N$  equations for each cell in the domain, where  $N$  is the number of coupled equations in the set. Because there are  $N$  equations per cell, this is sometimes called a "block" system of equations.

A point implicit linear equation solver (Incomplete Lower Upper (ILU) factorization scheme or a symmetric block Gauss-Seidel) is used in conjunction with an algebraic multigrid (AMG) method to solve the resultant block system of equations for all  $N$  dependent variables in each cell. For example, linearization of the coupled continuity,  $x$ -,  $y$ -,  $z$ -momentum, and energy equation set will produce a system of equations in which  $p$ ,  $u$ ,  $v$ ,  $w$ , and  $T$  are the unknowns. Simultaneous solution of this equation system (using the block AMG solver) yields at once updated pressure,  $u$ -,  $v$ -,  $w$ - velocity, and temperature fields.

In summary, the coupled implicit approach solves for all variables ( $p$ ,  $u$ ,  $v$ ,  $w$ ,  $T$ ) in all cells at the same time.

If you choose the explicit option of the density-based solver, each equation in the coupled set of governing equations is linearized explicitly. As in the implicit option, this too will result in a system of equations with  $N$  equations for each cell in the domain and likewise, all dependent variables in the set will be updated at once. However, this system of equations is explicit in the unknown dependent variables. For example, the  $x$ -momentum equation is written such that the updated  $x$  velocity is a function of existing values of the field variables. Because of this, a linear equation solver is not needed. Instead, the solution is updated using a multi-stage (Runge-Kutta) solver. Here you have the additional option of employing a full approximation storage (FAS) multigrid scheme to accelerate the multi-stage solver.

In summary, the density-based explicit approach solves for all variables ( $p$ ,  $u$ ,  $v$ ,  $w$ ,  $T$ ) one cell at a time.

### 4.3 Boundary Conditions used for different part of geometry

Parts	Boundary Conditions used
Nose	Wall
Body	Wall
Boat Tail	Wall
Exhaust Dia	Wall
Farfield	Pressure Farfield

Table 4.3 Boundary conditions used for different part of geometry

## 4.4 Flow Conditions

Part	Farfield	Exhaust BC(Pressure inlet BC	
Mach no.	0.15		
Initial Gauge Pressure(Pa)	-	121638	
Total Gauge Pressure(Pa)	101325	205727	
Velocity(m/s)	35		
Temperature(K)	303.15	956.33	
Density(Kg/m^3)	1.1638	-	

Table 4.4 Flow conditions

## CHAPTER 5

### RESULTS AND DISCUSSION

The analysis is done on ANSYS and Hi-FUN, the results are then extracted and post processed using Tecplot, Paraview and MS Excel.

#### 5.1. Cp distribution over the surface of the Missile body

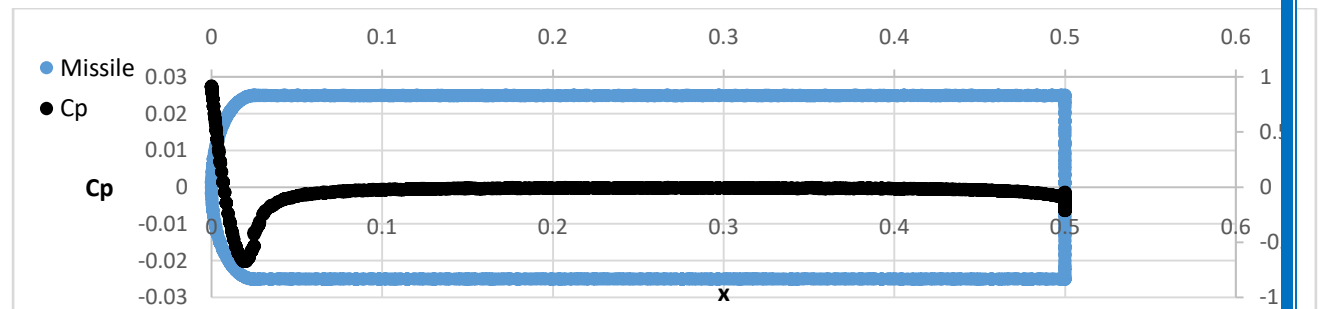


**Fig 5.1.1. Cp distribution on flat base**

The above graph shows the Cp distribution on the surface of the missile body for a flat base configuration at 0deg angle of attack and 50m/s. From the above graph we can clearly see that there is a pressure change on the surface of the missile this is because the velocity decreases at the nose and gradually increases and reaches a constant value at the body and at the base the flow reversal is shown by a black vertical line.

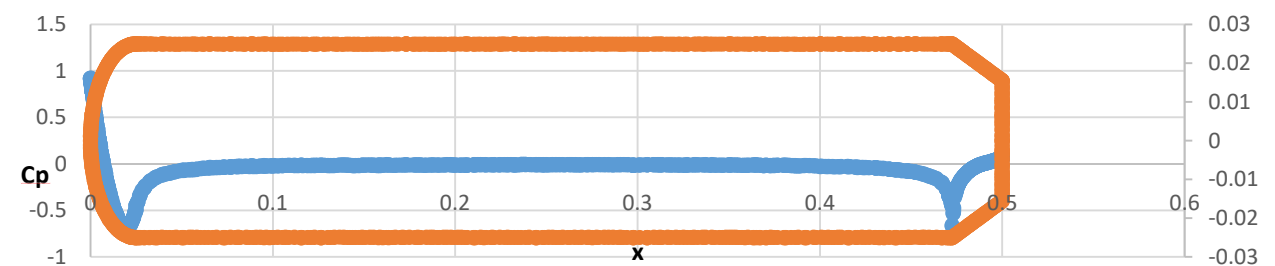


**Fig 5.1.2. Cp Distribution on the boat tail base**

The above graph shows the Cp distribution on the surface of the missile body for a boat tail base configuration at 0deg angle of attack and 50m/s. From the above graph we can clearly see that there is a pressure change on the surface of the missile this is because the velocity decreases at the nose and gradually increases and reaches a constant value at the body and thereafter there is a gradual decrease in the velocity decrease in velocity at the starting of the boat tail section and thereafter there is an increase in the velocity until the base section.

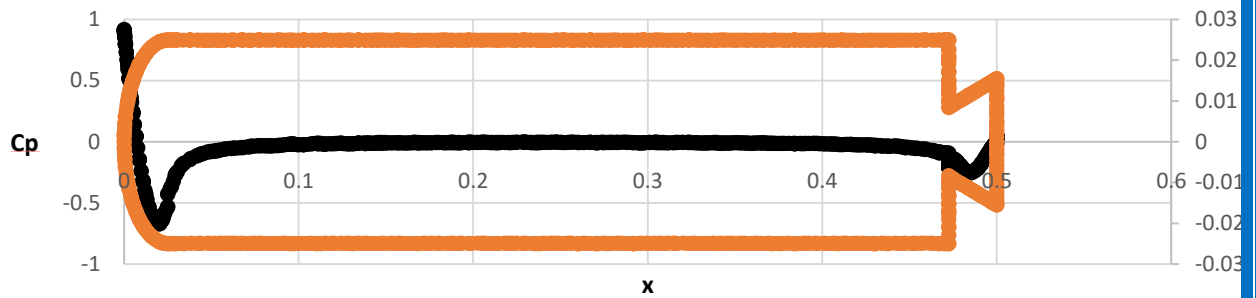


**Fig 5.1.3. Cp distribution on nozzle base**

The above graph shows the  $C_p$  distribution on the surface of the missile body for a nozzle base configuration at  $0^\circ$  angle of attack and  $50\text{ m/s}$ . From the above graph we can clearly see that there is a pressure change on the surface of the missile this is because the velocity decreases at the nose and gradually increases and reaches a constant value at the body and thereafter there is a gradual decrease in the velocity decrease in velocity at the starting of the boat tail section and thereafter there is an increase in the velocity until the base section.

From the above three graphs it can be clearly noticed that there is only difference in the pressure distribution on the base part and the pressure distribution at the body remains constant.

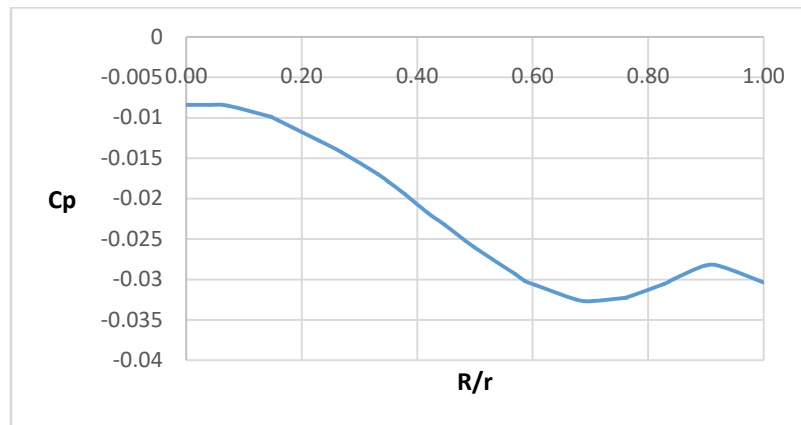


**Fig 5.1.4. Cp along the base of flat base at  $0^\circ$  AoA ( $20\text{ m/s}$ )**

The above graph shows the  $C_p$  distribution along the base of the missile for a flat base configuration at  $20\text{ m/s}$  and  $0^\circ$  angle of attack. From the above graph it can be clearly seen that the pressure is the least at the center of the base and the pressure gradually increases as we move away from the center. This gradual decrease in the pressure causes flow reversal.



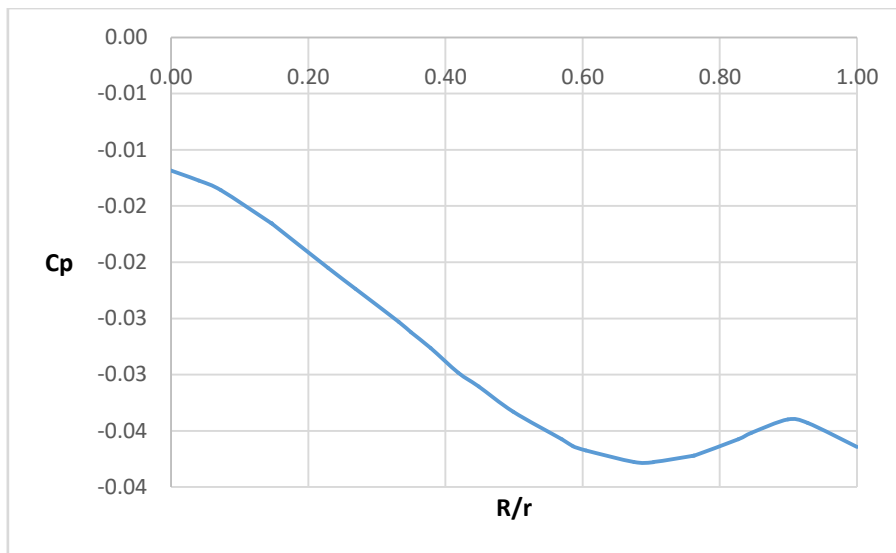


**Fig 5.1.5.  $C_p$  along flatbase at 2 AoA (20 m/s)**

The above graph shows the  $C_p$  distribution along the base of the missile for a flat base configuration at 20m/s and 2deg angle of attack. From the above graph it can be clearly seen that the pressure is the least at the center of the base and the pressure gradually increases as we move away from the center. This gradual decrease in the pressure causes flow reversal.

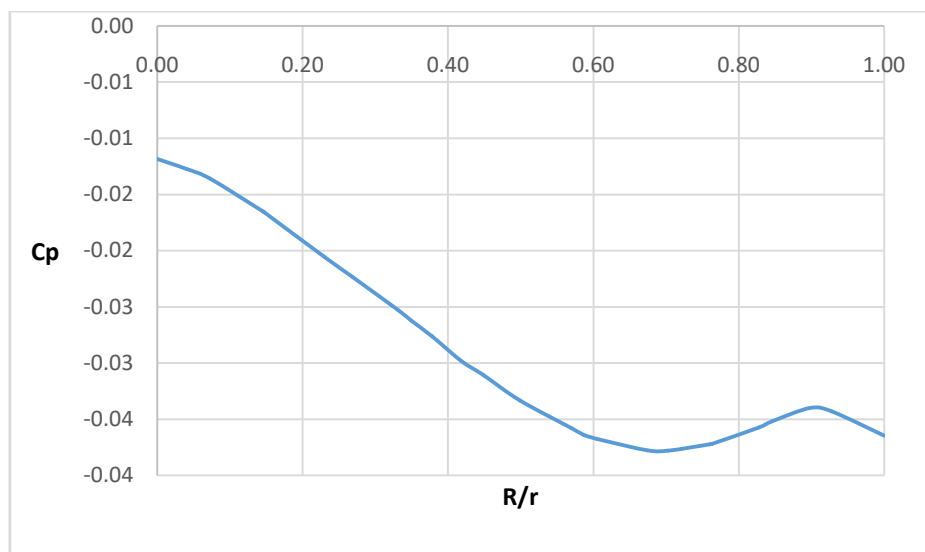


**Fig 5.1.6.  $C_p$  along flatbase at -2 AoA (20m/s)**

The above graph shows the  $C_p$  distribution along the base of the missile for a flat base configuration at 20m/s and -2deg angle of attack. From the above graph it can be clearly seen that the pressure is the least at the center of the base and the pressure gradually increases as we move away from the center. This gradual decrease in the pressure causes flow reversal.

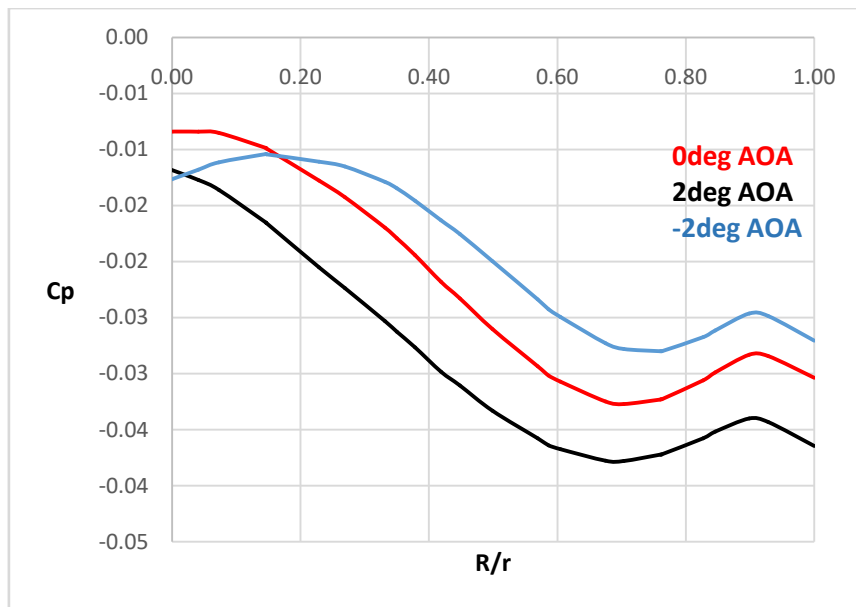


**Fig 5.1.7. Comparison of  $C_p$  of flatbase for different AoA at 20 m/s**

The above graph shows the  $C_p$  distribution for a flat base configuration at 20m/s for different angle of attack. From the above graph we can observe that the peak of the graph shifts as the angle of attack changes, the grave shifts to the left as we increase the angle of attack, to the right as we decrease the angle of attack and at the center for 0deg angle of attack.

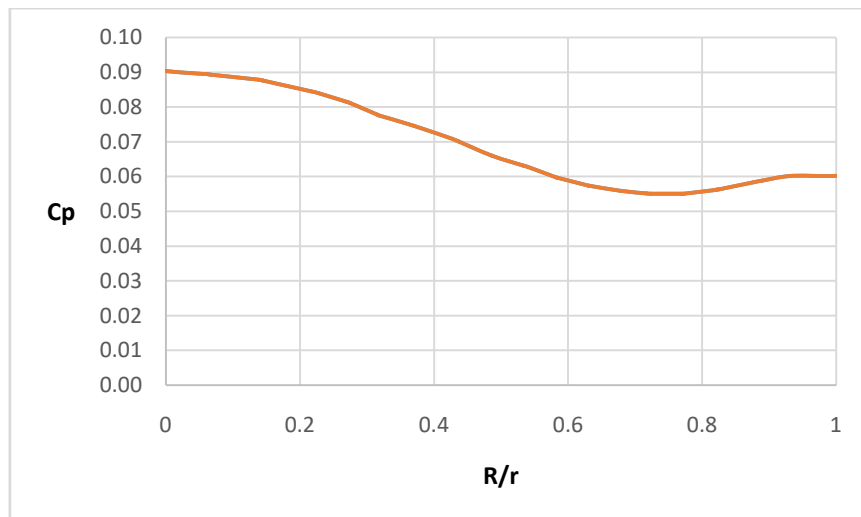


**Fig 5.1.8.  $C_p$  along boattail at 0 AoA (20 m/s)**

The above graph shows the  $C_p$  distribution along the base of the missile for a boat tail base configuration at 20m/s and 0deg angle of attack. From the above graph it can be clearly seen that the pressure is the least at the center of the base and the pressure gradually increases as we move away from the center. This gradual decrease in the pressure causes flow reversal.

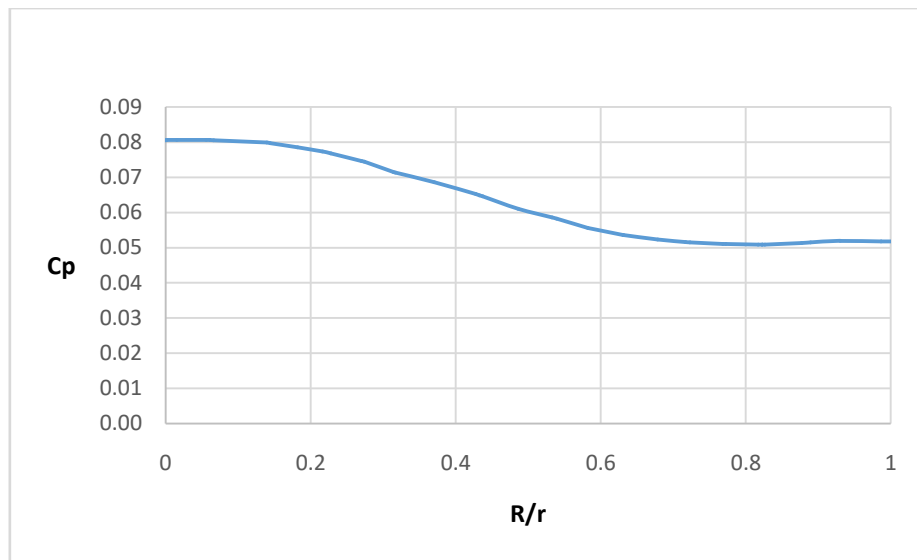


**Fig 5.1.9. Cp along boattail at 2 AoA (20 m/s)**

The above graph shows the  $C_p$  distribution along the base of the missile for a boat tail base configuration at 20m/s and 2deg angle of attack. From the above graph it can be clearly seen that the pressure is the least at the center of the base and the pressure gradually increases as we move away from the center. This gradual decrease in the pressure causes flow reversal.

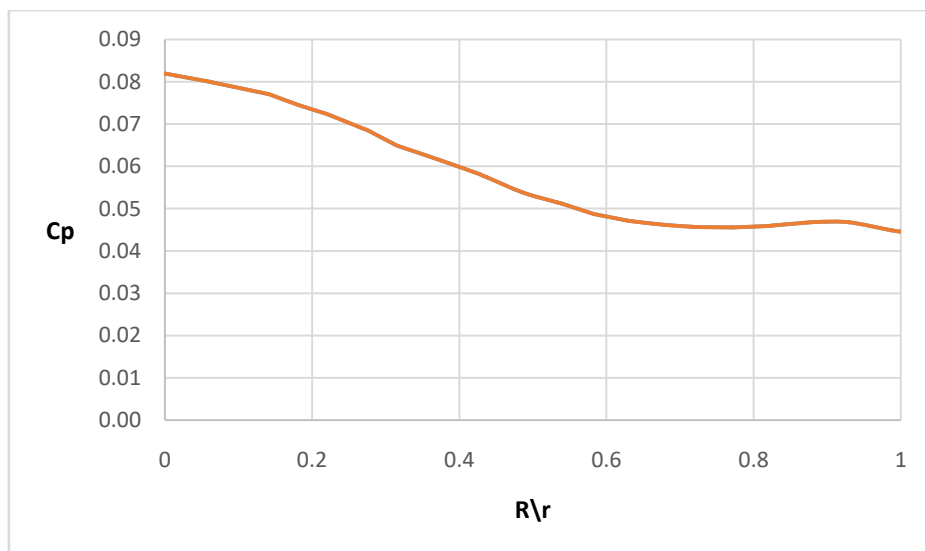


**Fig 5.1.10.Cp along boattail at -2 AoA (20 m/s)**

The above graph shows the  $C_p$  distribution along the base of the missile for a boat tail base configuration at 20m/s and -2deg angle of attack. From the above graph it can be clearly seen that the pressure is the least at the center of the base and the pressure gradually increases as we move away from the center. This gradual decrease in the pressure causes flow reversal.

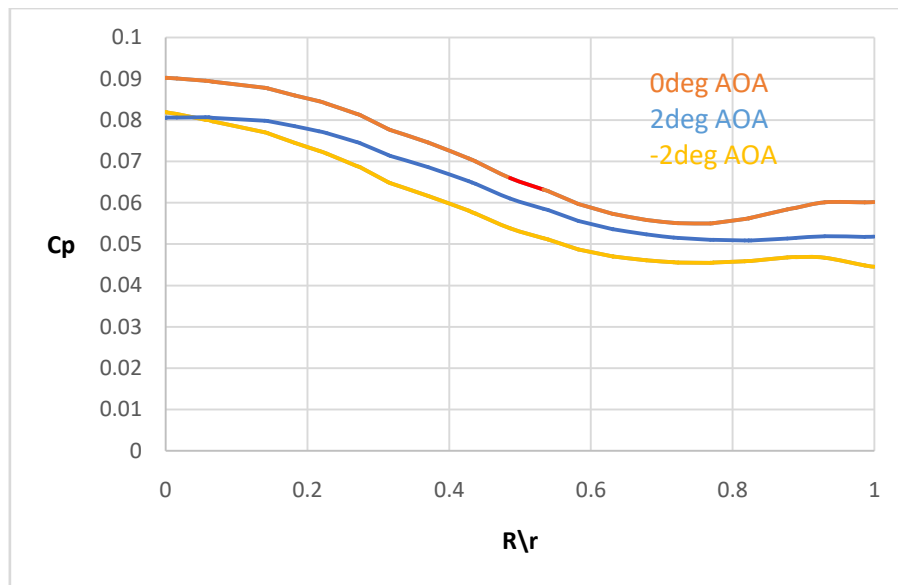


**Fig 5.1.11. Comparison of Cp of boattail base for different AoA at 20 m/s**

The above graph shows the Cp distribution for a boat tail base configuration at 20m/s for different angle of attack. From the above graph we can observe that the peak of the graph shifts as the angle of attack changes, the grave shifts to the left as we increase the angle of attack, to the right as we decrease the angle of attack and at the center for 0deg angle of attack.

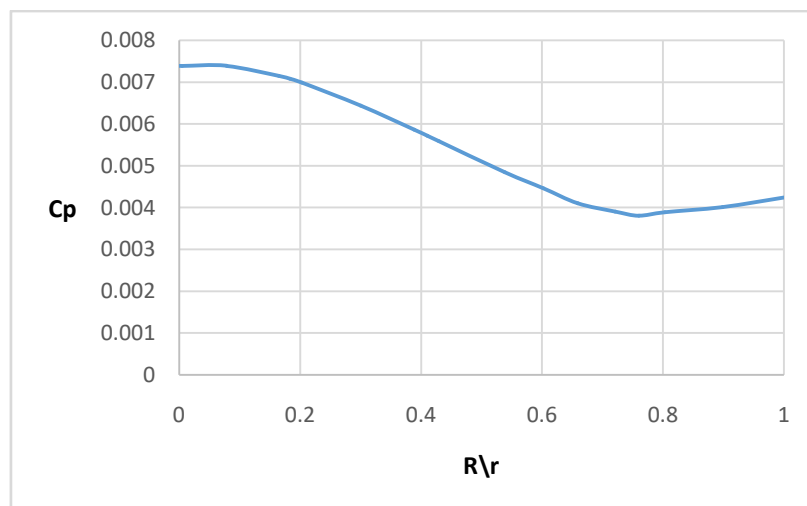


**Fig 5.1.12. Cp along nozzle base at 0 AoA (20 m/s)**

The above graph shows the Cp distribution along the base of the missile for a nozzle base configuration at 20m/s and 0deg angle of attack. From the above graph it can be clearly seen that the pressure is the least at the center of the base and the pressure gradually increases as we move away from the center. This gradual decrease in the pressure causes flow reversal.

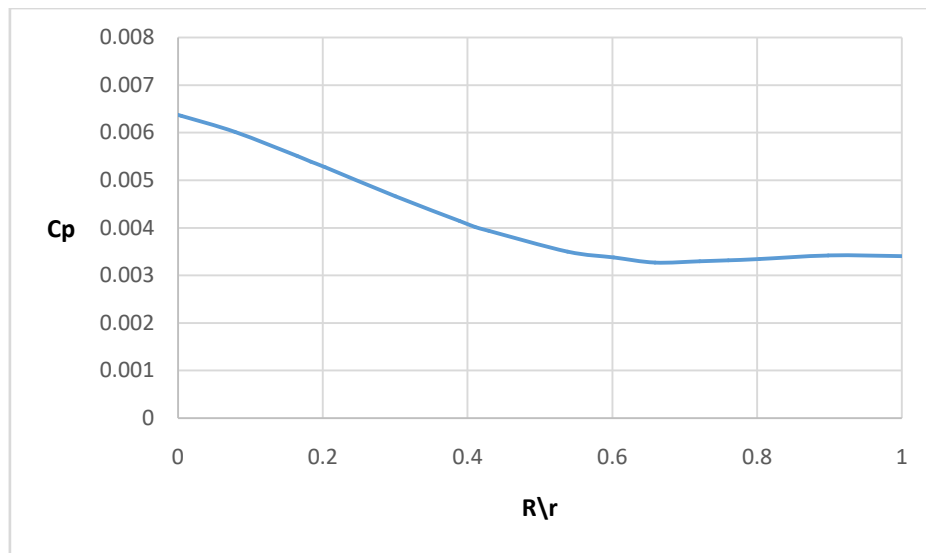


**Fig 5.1.13.Cp along nozzle base at 2 AoA (20 m/s)**

The above graph shows the  $C_p$  distribution along the base of the missile for a nozzle base configuration at 20m/s and 2deg angle of attack. From the above graph it can be clearly seen that the pressure is the least at the center of the base and the pressure gradually increases as we move away from the center. This gradual decrease in the pressure causes flow reversal.

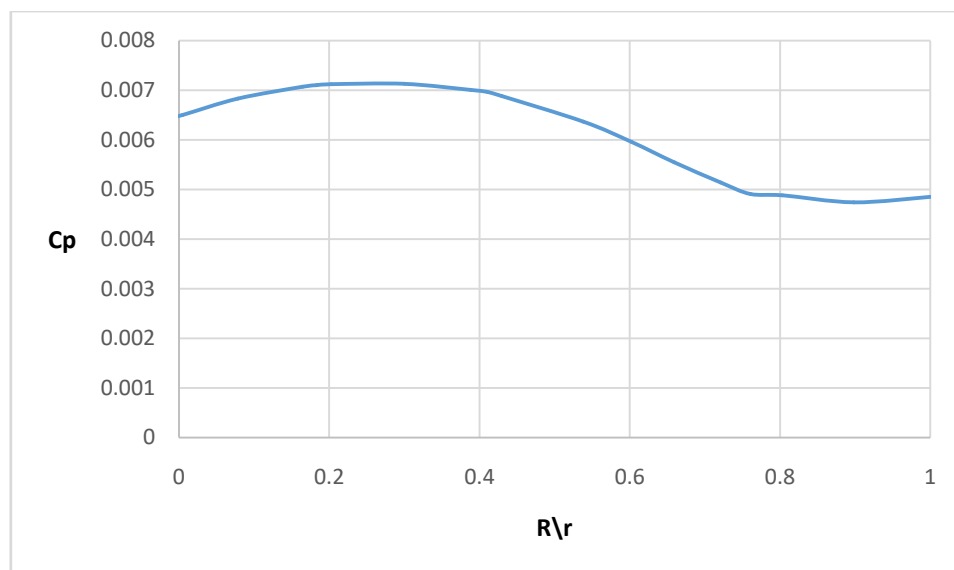


**Fig 5.1.14.Cp along nozzle base at -2 AoA (20 m/s)**

The above graph shows the  $C_p$  distribution along the base of the missile for a nozzle base configuration at 20m/s and -2deg angle of attack. From the above graph it can be clearly seen that the pressure is the least at the center of the base and the pressure gradually increases as we move away from the center. This gradual decrease in the pressure causes flow reversal.

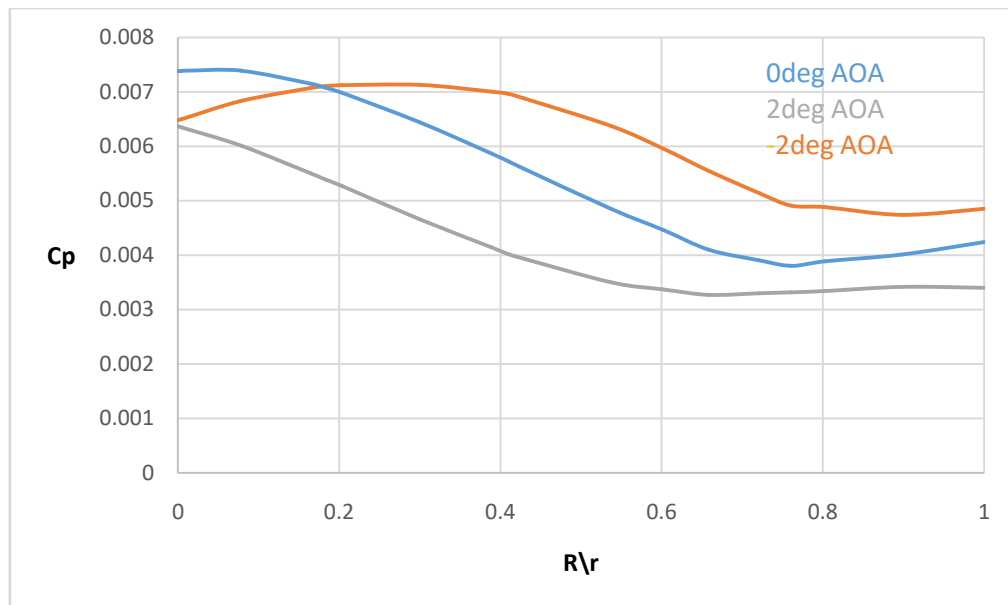


**Fig 5.1.15. Comparison of Cp of nozzle base for different AoA at 20 m/s**

The above graph shows the Cp distribution for a nozzle base configuration at 20m/s for different angle of attack. From the above graph we can observe that the peak of the graph shifts as the angle of attack changes, the curve shifts to the left as we increase the angle of attack, to the right as we decrease the angle of attack and at the center for 0deg angle of attack.

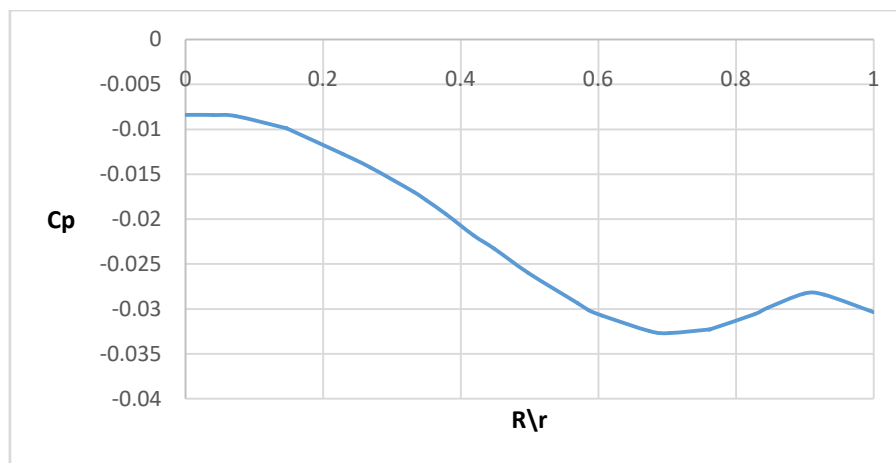


**Fig 5.1.16. Cp along flatbase at 0 AoA (35 m/s)**

The above graph shows the Cp distribution along the base of the missile for a flat base configuration at 35m/s and 0deg angle of attack. From the above graph it can be clearly seen that the pressure is the least at the center of the base and the pressure gradually increases as we move away from the center. This gradual decrease in the pressure causes flow reversal.

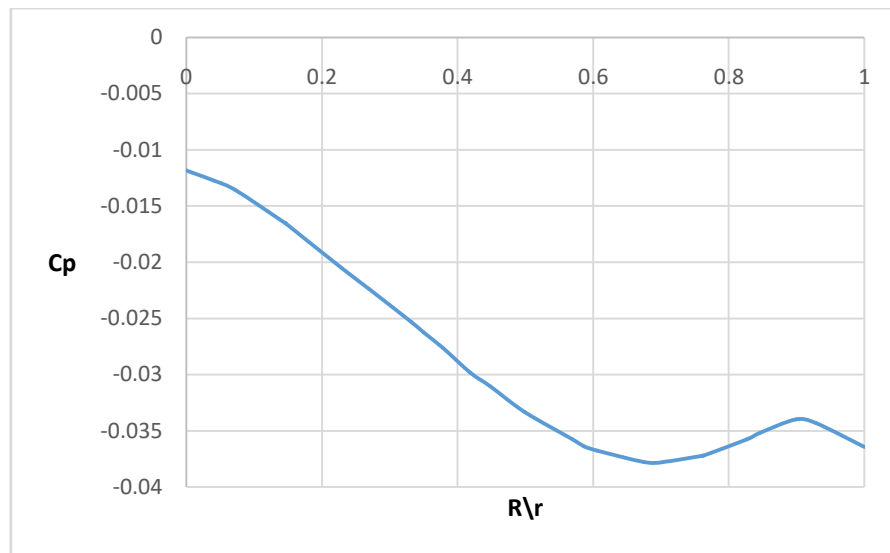


**Fig 5.1.17.  $C_p$  along flat base at 2 AoA (35 m/s)**

The above graph shows the  $C_p$  distribution along the base of the missile for a flat base configuration at 35m/s and 2deg angle of attack. From the above graph it can be clearly seen that the pressure is the least at the center of the base and the pressure gradually increases as we move away from the center. This gradual decrease in the pressure causes flow reversal.

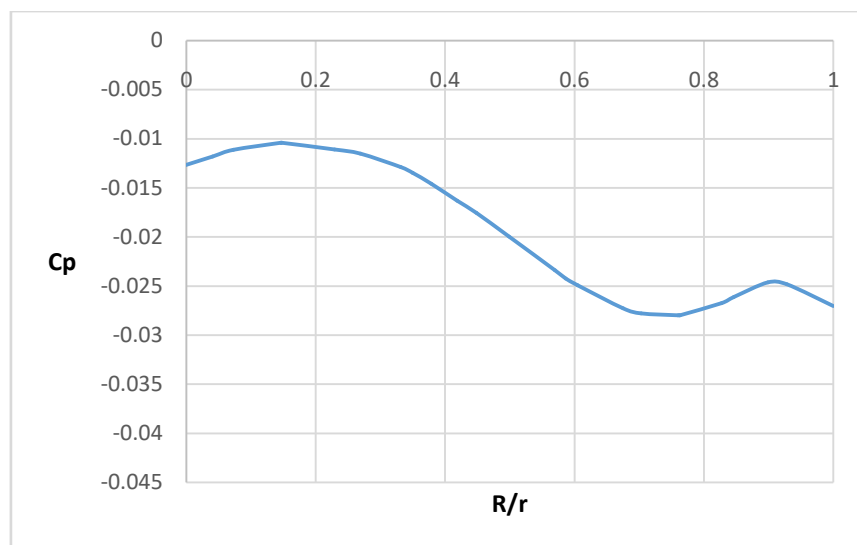


**Fig 5.1.18.  $C_p$  along flat base at -2 AoA (35 m/s)**

The above graph shows the  $C_p$  distribution along the base of the missile for a flat base configuration at 35m/s and -2deg angle of attack. From the above graph it can be clearly seen that the pressure is the least at the center of the base and the pressure gradually increases as we move away from the center. This gradual decrease in the pressure causes flow reversal.

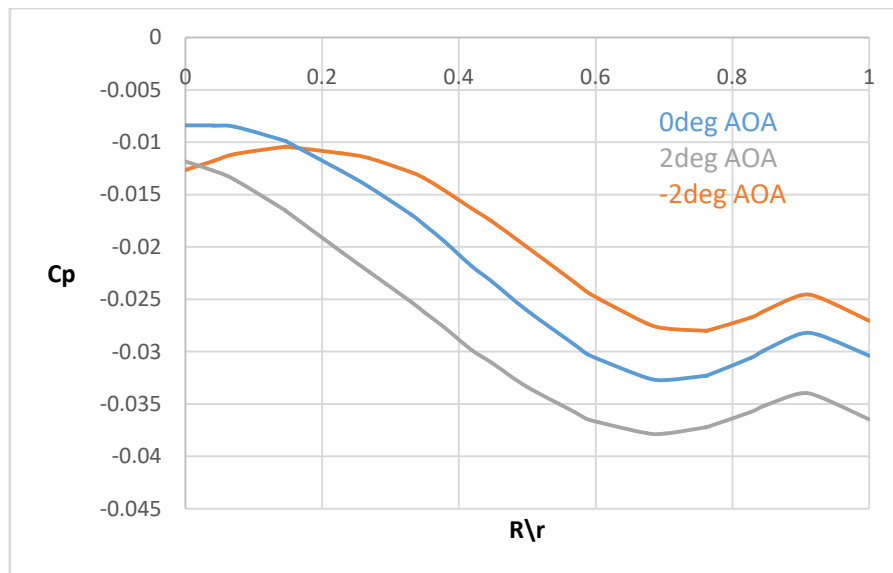


**Fig 5.1.19. Comparison of Cp of flat base for different AoA at 35 m/s**

The above graph shows the Cp distribution for a flat base configuration at 35m/s for different angle of attack. From the above graph we can observe that the peak of the graph shifts as the angle of attack changes, the grave shifts to the left as we increase the angle of attack, to the right as we decrease the angle of attack and at the center for 0deg angle of attack.

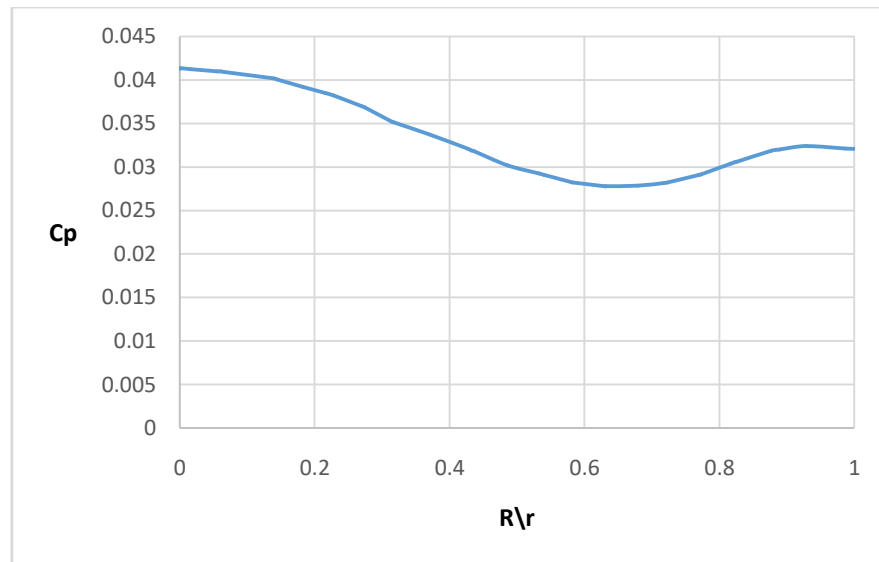


**Fig 5.1.20.Cp along boat tail base at 0 AoA (35 m/s)**

The above graph shows the Cp distribution along the base of the missile for a boat tail base configuration at 35m/s and 0deg angle of attack. From the above graph it can be clearly seen that the pressure is the least at the center of the base and the pressure gradually increases as we move away from the center. This gradual decrease in the pressure causes flow reversal.



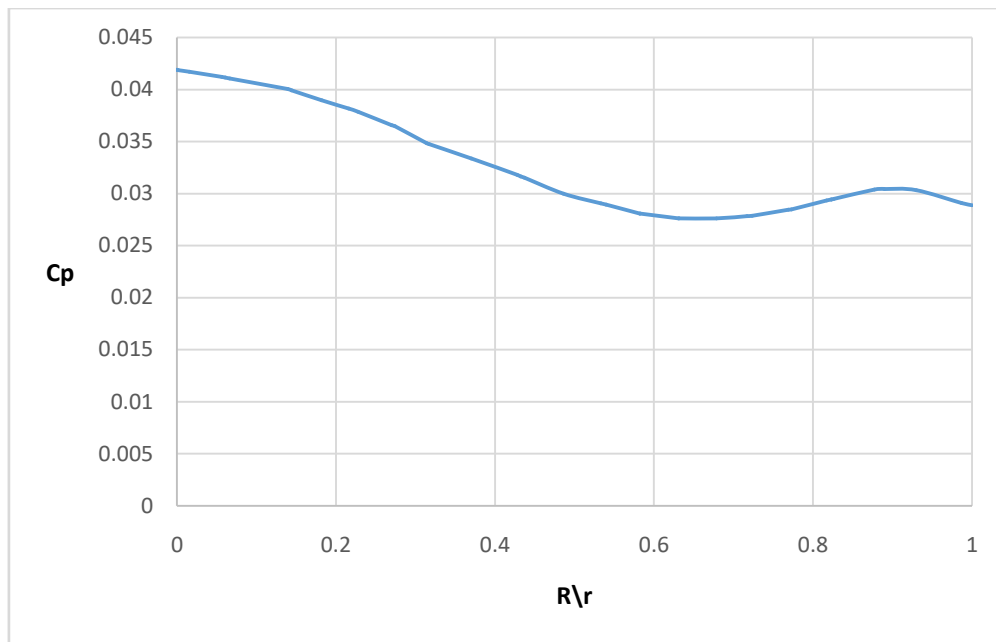


**Fig 5.1.21.Cp along flat base at 2 AoA (35 m/s)**

The above graph shows the  $C_p$  distribution along the base of the missile for a boat tail base configuration at 35m/s and 2deg angle of attack. From the above graph it can be clearly seen that the pressure is the least at the center of the base and the pressure gradually increases as we move away from the center. This gradual decrease in the pressure causes flow reversal.

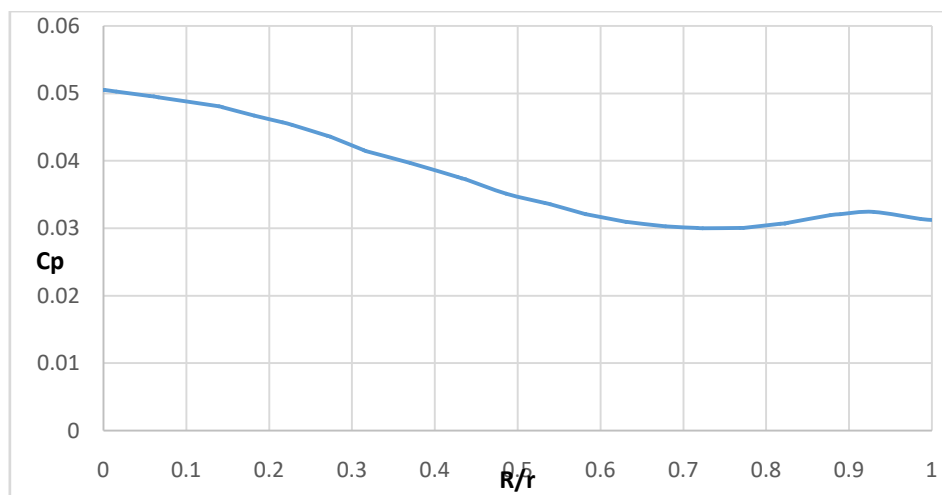


**Fig 5.1.22.Cp along flat base at -2 AoA (35 m/s)**

The above graph shows the  $C_p$  distribution along the base of the missile for a boat tail base configuration at 35m/s and -2deg angle of attack. From the above graph it can be clearly seen that the pressure is the least at the center of the base and the pressure gradually increases as we move away from the center. This gradual decrease in the pressure causes flow reversal.

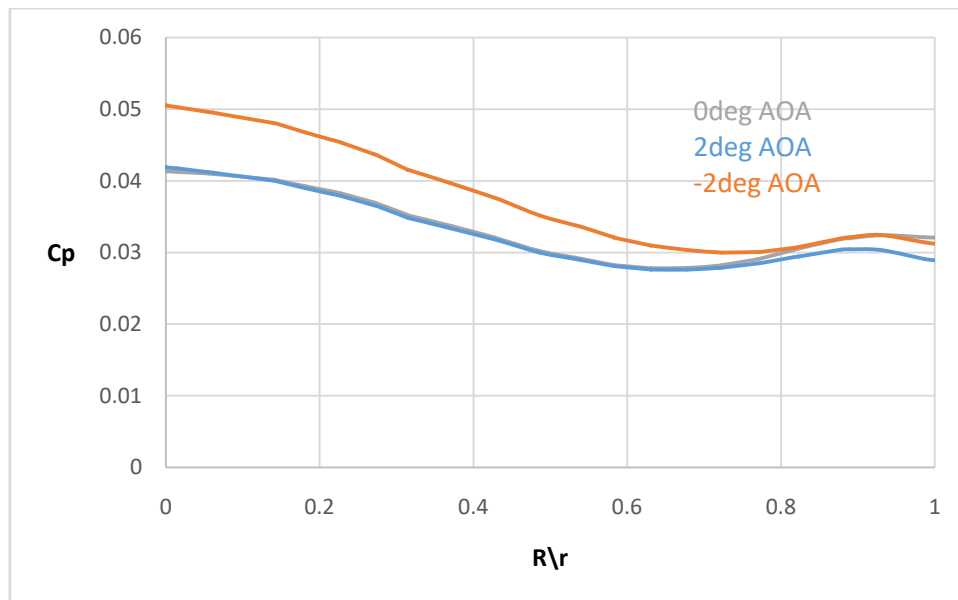


**Fig 5.1.23. Comparison of Cp of boat tail base for different AoA at 35 m/s**

The above graph shows the Cp distribution for a boat tail base configuration at 35m/s for different angle of attack. From the above graph we can observe that the peak of the graph shifts as the angle of attack changes, the grave shifts to the left as we increase the angle of attack, to the right as we decrease the angle of attack and at the center for 0deg angle of attack.

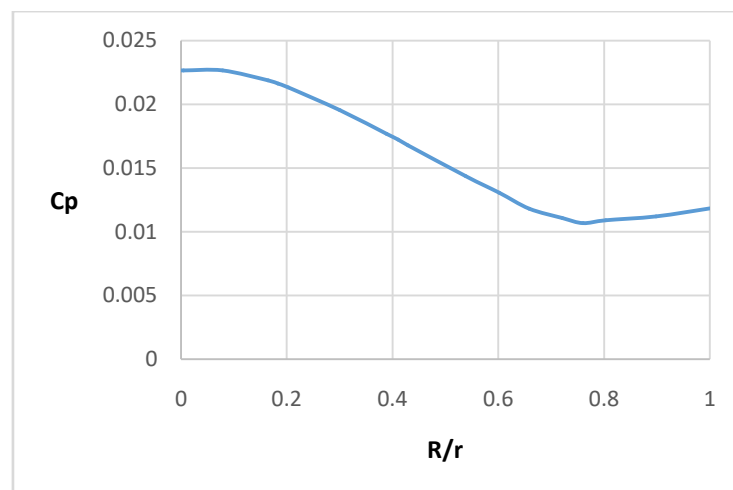


**Fig 5.1.24.Cp along nozzle base at 0 AoA (35 m/s)**

The above graph shows the Cp distribution along the base of the missile for a nozzle base configuration at 35m/s and 0deg angle of attack. From the above graph it can be clearly seen that the pressure is the least at the center of the base and the pressure gradually increases as we move away from the center. This gradual decrease in the pressure causes flow reversal.

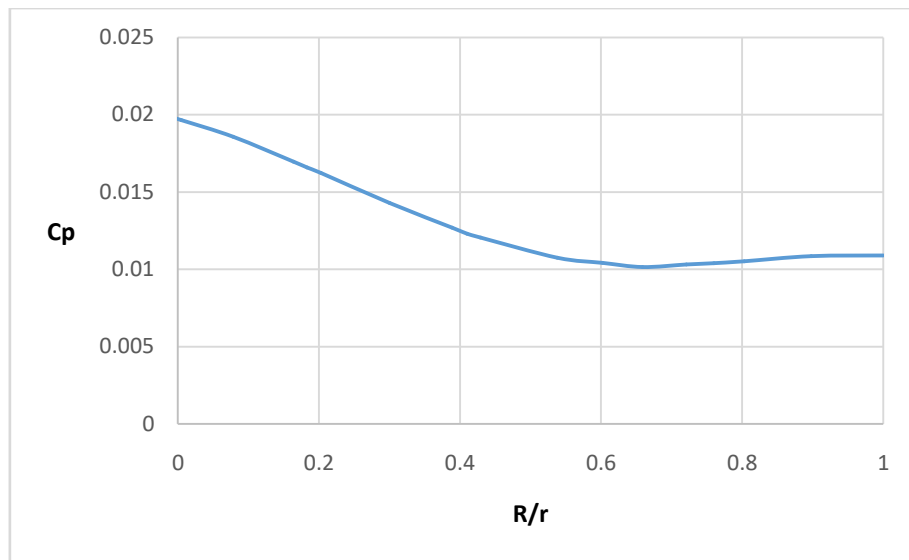


**Fig 5.1.25.Cp along nozzle base at 2 AoA (35 m/s)**

The above graph shows the  $C_p$  distribution along the base of the missile for a nozzle base configuration at 35m/s and 2deg angle of attack. From the above graph it can be clearly seen that the pressure is the least at the center of the base and the pressure gradually increases as we move away from the center. This gradual decrease in the pressure causes flow reversal.

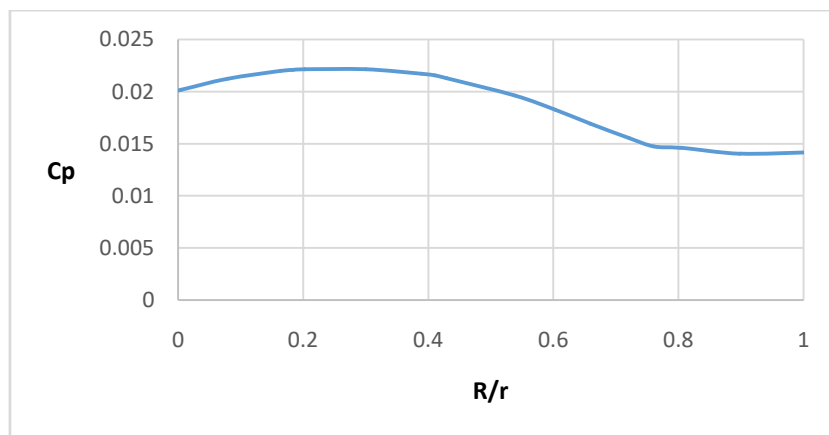


**Fig 5.1.26.Cp along nozzle base at -2 AoA (35 m/s)**

The above graph shows the  $C_p$  distribution along the base of the missile for a nozzle base configuration at 35m/s and -2deg angle of attack. From the above graph it can be clearly seen that the pressure is the least at the center of the base and the pressure gradually increases as we move away from the center. This gradual decrease in the pressure causes flow reversal.

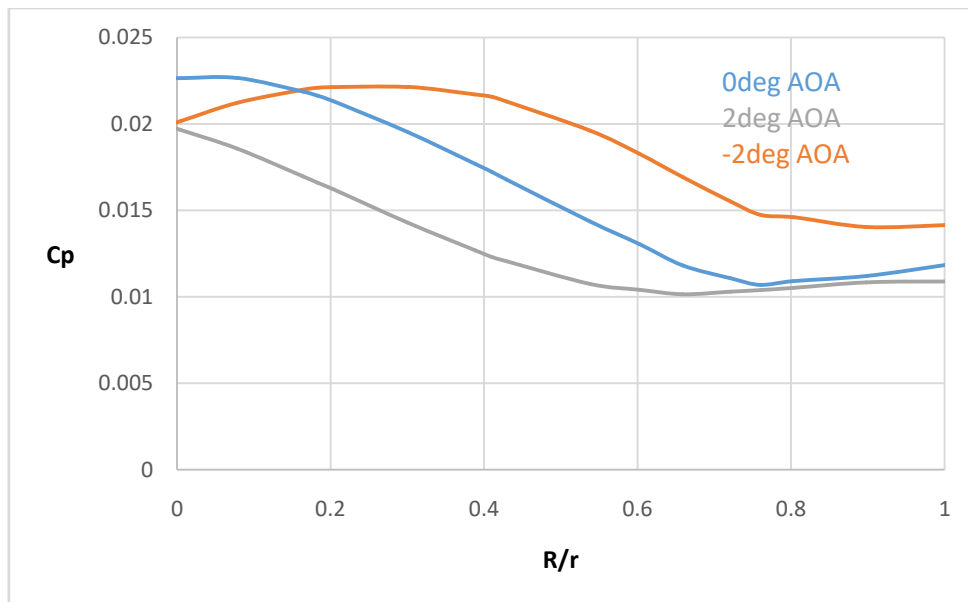


**Fig 5.1.27. Comparison of Cp of nozzle tail base for different AoA at 35 m/s**

The above graph shows the Cp distribution for a nozzle base configuration at 35m/s for different angle of attack. From the above graph we can observe that the peak of the graph shifts as the angle of attack changes, the curve shifts to the left as we increase the angle of attack, to the right as we decrease the angle of attack and at the center for 0deg angle of attack.

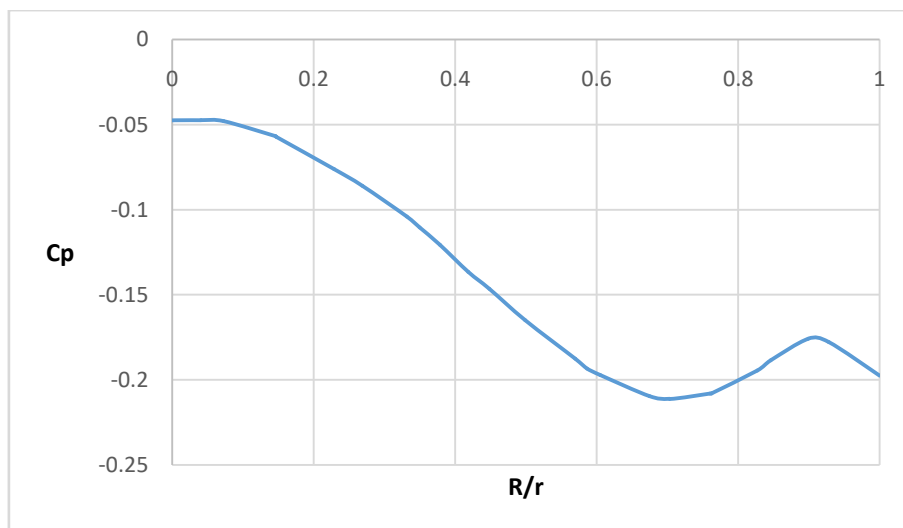


**Fig 5.1.28. Cp along flat base at 0 AoA (50 m/s)**

The above graph shows the Cp distribution along the base of the missile for a flat base configuration at 50m/s and 0deg angle of attack. From the above graph it can be clearly seen that the pressure is the least at the center of the base and the pressure gradually increases as we move away from the center. This gradual decrease in the pressure causes flow reversal.

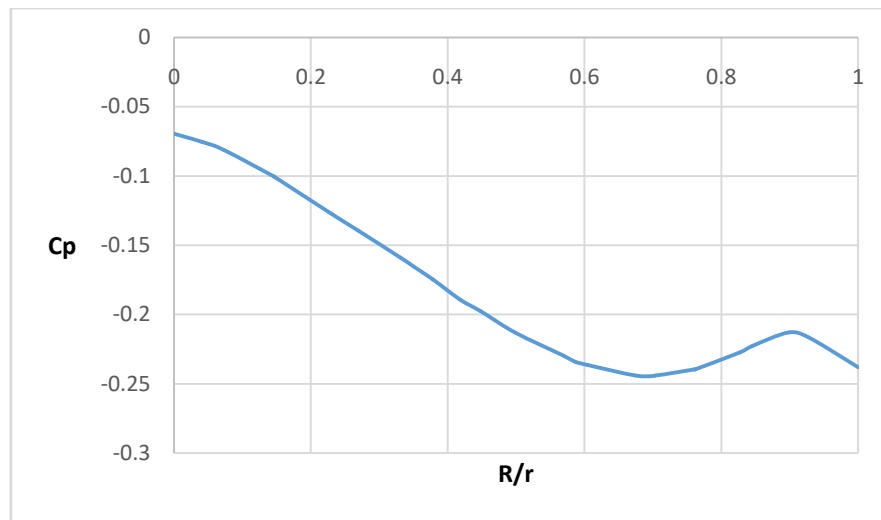


**Fig 5.1.29.  $C_p$  along flat base at 2 AoA (50 m/s)**

The above graph shows the  $C_p$  distribution along the base of the missile for a flat base configuration at 50m\s and 2deg angle of attack. From the above graph it can be clearly seen that the pressure is the least at the center of the base and the pressure gradually increases as we move away from the center. This gradual decrease in the pressure causes flow reversal.

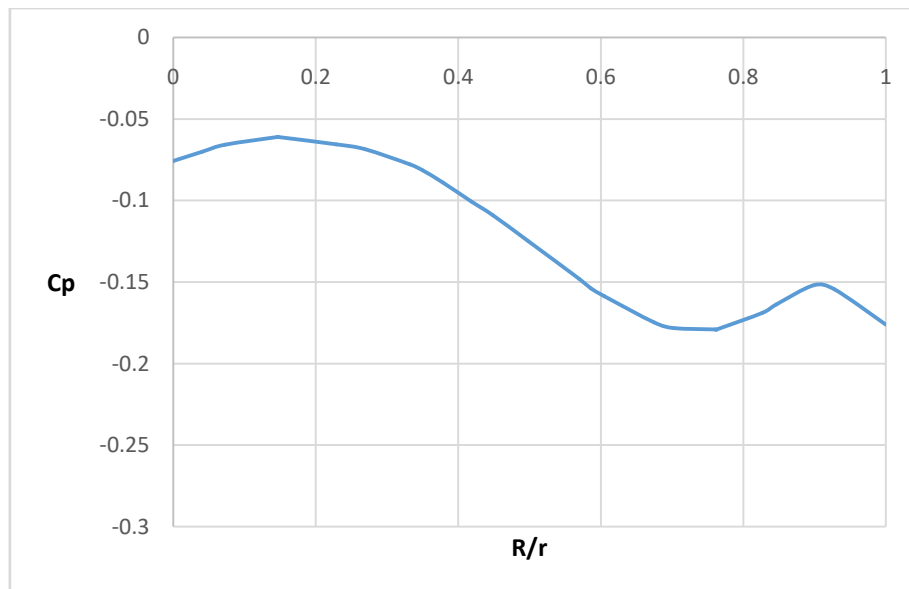


**Fig 5.1.30.  $C_p$  along flat base at -2 AoA (50 m/s)**

The above graph shows the  $C_p$  distribution along the base of the missile for a flat base configuration at 50m\s and -2deg angle of attack. From the above graph it can be clearly seen that the pressure is the least at the center of the base and the pressure gradually increases as we move away from the center. This gradual decrease in the pressure causes flow reversal.

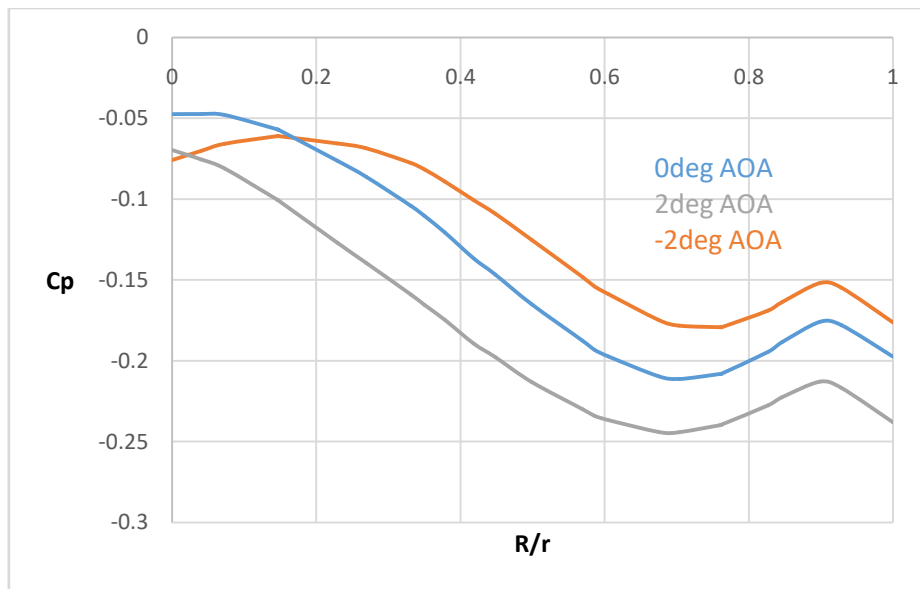


**Fig 5.1.31. Comparison of  $C_p$  of flat tail base for different AoA at 50 m/s**

The above graph shows the  $C_p$  distribution for a flat base configuration at 50m/s for different angle of attack. From the above graph we can observe that the peak of the graph shifts as the angle of attack changes, the grave shifts to the left as we increase the angle of attack, to the right as we decrease the angle of attack and at the center for 0deg angle of attack.

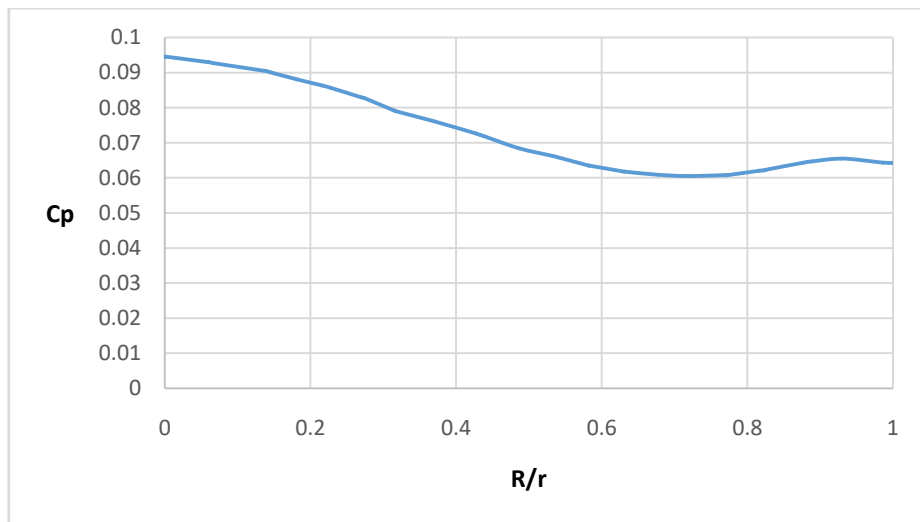


**Fig 5.1.32.  $C_p$  along boat tail base at 0 AoA (50 m/s)**

The above graph shows the  $C_p$  distribution along the base of the missile for a boat tail base configuration at 50m/s and 0deg angle of attack. From the above graph it can be clearly seen that the pressure is the least at the center of the base and the pressure gradually increases as we move away from the center. This gradual decrease in the pressure causes flow reversal

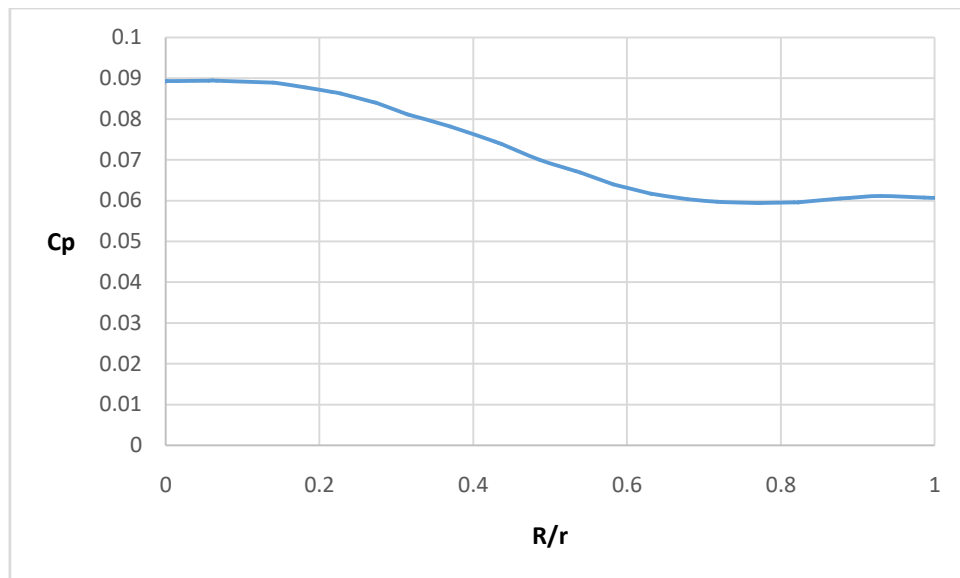


**Fig 5.1.33.Cp along boat tail base at 2 AoA (50 m/s)**

The above graph shows the  $C_p$  distribution along the base of the missile for a boat tail base configuration at 50m/s and 2deg angle of attack. From the above graph it can be clearly seen that the pressure is the least at the center of the base and the pressure gradually increases as we move away from the center. This gradual decrease in the pressure causes flow reversal.

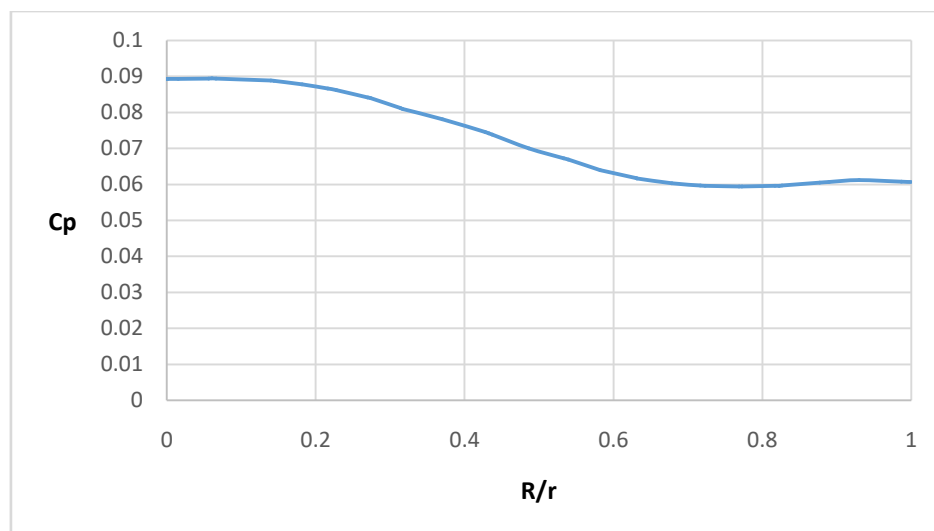


**Fig 5.1.34.Cp along boat tail base at -2 AoA (50 m/s)**

The above graph shows the  $C_p$  distribution along the base of the missile for a boat tail base configuration at 50m/s and -2deg angle of attack. From the above graph it can be clearly seen that the pressure is the least at the center of the base and the pressure gradually increases as we move away from the center. This gradual decrease in the pressure causes flow reversal.

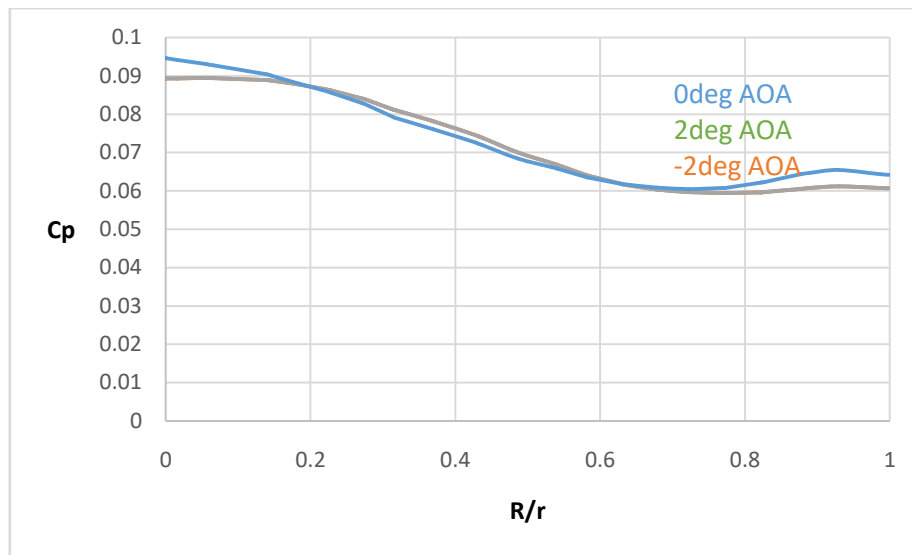


**Fig 5.1.35. Comparison of  $C_p$  of boat tail base for different AoA at 50 m/s**

The above graph shows the  $C_p$  distribution for a boat tail base configuration at 50m/s for different angle of attack. From the above graph we can observe that the peak of the graph shifts as the angle of attack changes, the grave shifts to the left as we increase the angle of attack, to the right as we decrease the angle of attack and at the center for 0deg angle of attack.

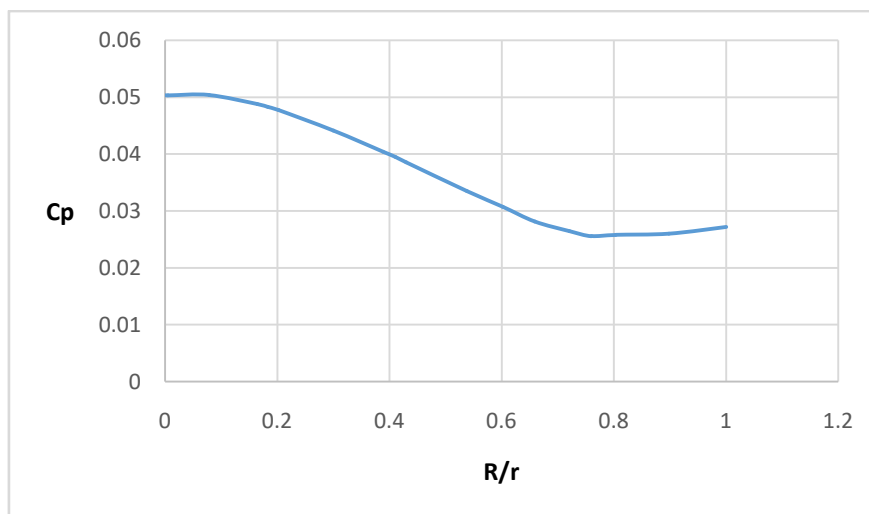


**Fig 5.1.36.  $C_p$  along nozzle base at 0 AoA (50 m/s)**

The above graph shows the  $C_p$  distribution along the base of the missile for a nozzle base configuration at 50m/s and 0deg angle of attack. From the above graph it can be clearly seen that the pressure is the least at the center of the base and the pressure gradually increases as we move away from the center. This gradual decrease in the pressure causes flow reversal.



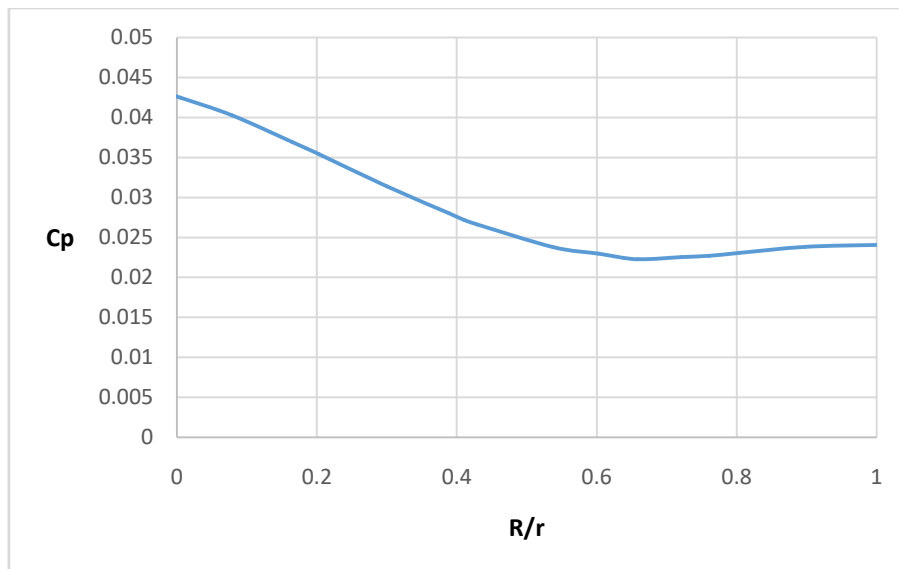


**Fig 5.1.37.  $C_p$  along nozzle base at 2 AoA (50 m/s)**

The above graph shows the  $C_p$  distribution along the base of the missile for a nozzle base configuration at 50m\s and 2deg angle of attack. From the above graph it can be clearly seen that the pressure is the least at the center of the base and the pressure gradually increases as we move away from the center. This gradual decrease in the pressure causes flow reversal.

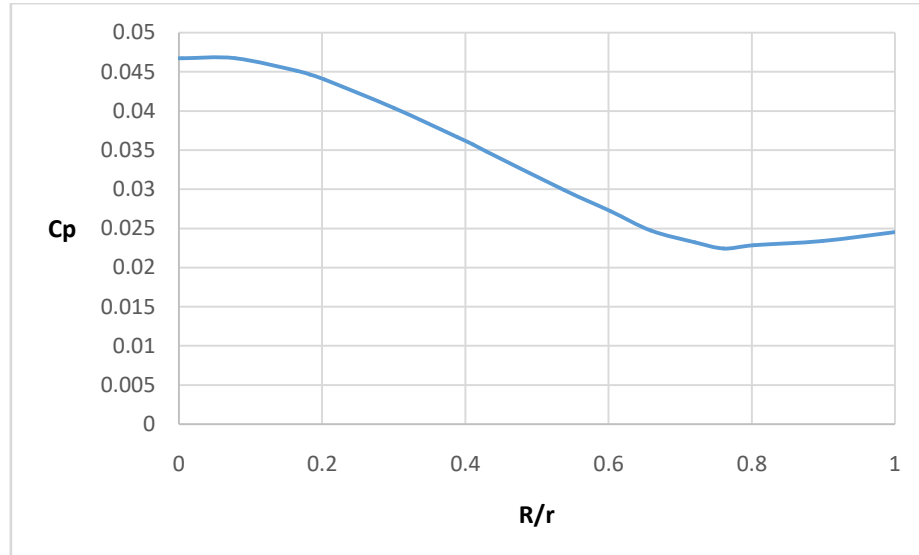


**Fig 5.1.38.  $C_p$  along Nozzle base at -2 AoA (50 m/s)**

The above graph shows the  $C_p$  distribution along the base of the missile for a nozzle base configuration at 50m\s and -2deg angle of attack. From the above graph it can be clearly seen that the pressure is the least at the center of the base and the pressure gradually increases as we move away from the center. This gradual decrease in the pressure causes flow reversal.

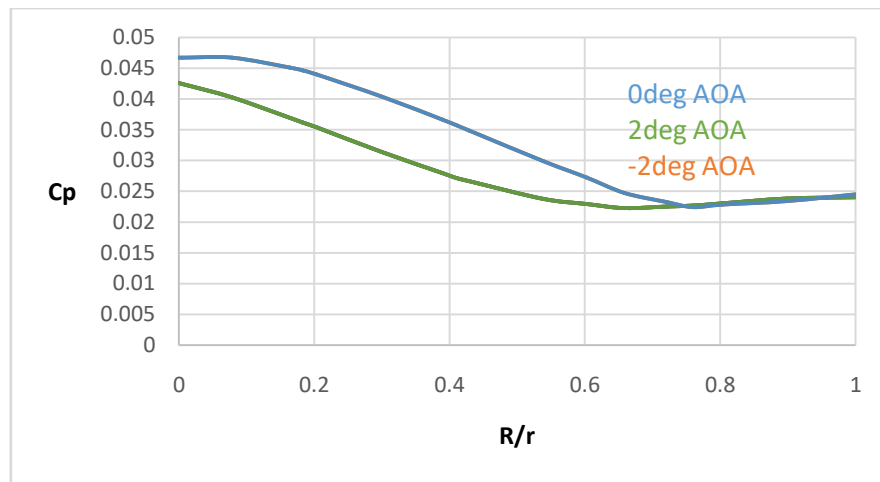


**Fig 5.1.39. Comparison of Cp of Nozzle base for different AoA at 50 m/s**

The above graph shows the Cp distribution for a nozzle base configuration at 50m/s for different angle of attack. From the above graph we can observe that the peak of the graph shifts as the angle of attack changes, the graph shifts to the left as we increase the angle of attack, to the right as we decrease the angle of attack and at the center for 0deg angle of attack.

## 5.2. Estimated drag values

Case	Velocity	Angle of attack	Cd (at base)
Flat base	20m/s	0deg	0.0792
Boat tail base	20m/s	0deg	0.0421
Nozzle base	20m/s	0deg	0.0678
Flat base	20m/s	2deg	0.0806
Boat tail base	20m/s	2deg	0.0429
Nozzle base	20m/s	2deg	0.0682
Flat base	20m/s	-2deg	0.0805
Boat tail base	20m/s	-2deg	0.0428
Nozzle base	20m/s	-2deg	0.0681
Flat base	35m/s	0deg	0.0763
Boat tail base	35m/s	0deg	0.0411
Nozzle base	35m/s	0deg	0.0678
Flat base	35m/s	2deg	0.0774
Boat tail base	35m/s	2deg	0.0412
Nozzle base	35m/s	2deg	0.0685
Flat base	35m/s	-2deg	0.0774
Boat tail base	35m/s	-2deg	0.0412
Nozzle base	35m/s	-2deg	0.0685
Flat base	50m/s	0deg	0.0759

Boat tail base	50m/s	0deg	0.0401
Nozzle base	50m/s	0deg	0.0674
Flat base	50m/s	2deg	0.0769
Boat tail base	50m/s	2deg	0.0403
Nozzle base	50m/s	2deg	0.068
Flat base	50m/s	-2deg	0.077
Boat tail base	50m/s	-2deg	0.0403
Nozzle base	50m/s	-2deg	0.0681

**Table 5.2 Estimated drag values**

The above table shows the estimated values of  $C_d$  (coefficient of drag) for all three configurations at different angle of attack and velocities.

### 5.3. $C_d$ plots for different angle of attack

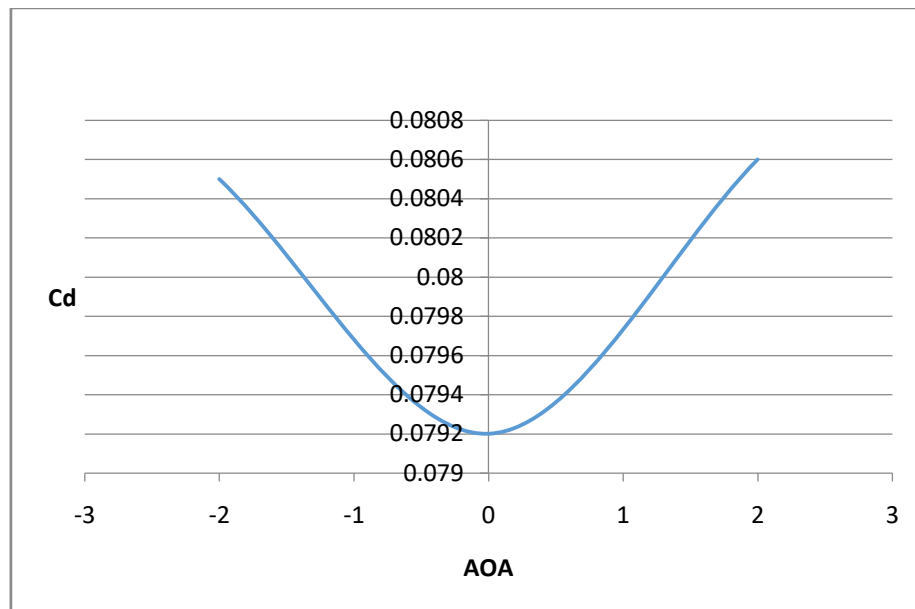


**Fig 5.3.1  $C_d$  of flat base for different AoA at 20 m/s**

The above graph shows the coefficient of drag for different angle of attack for a flat base configuration at 20m/s. From the graph it can be noted that the drag value increases with a change in the angle of attack, it can also be noted that at 0deg angle of attack the least value of drag is obtained.

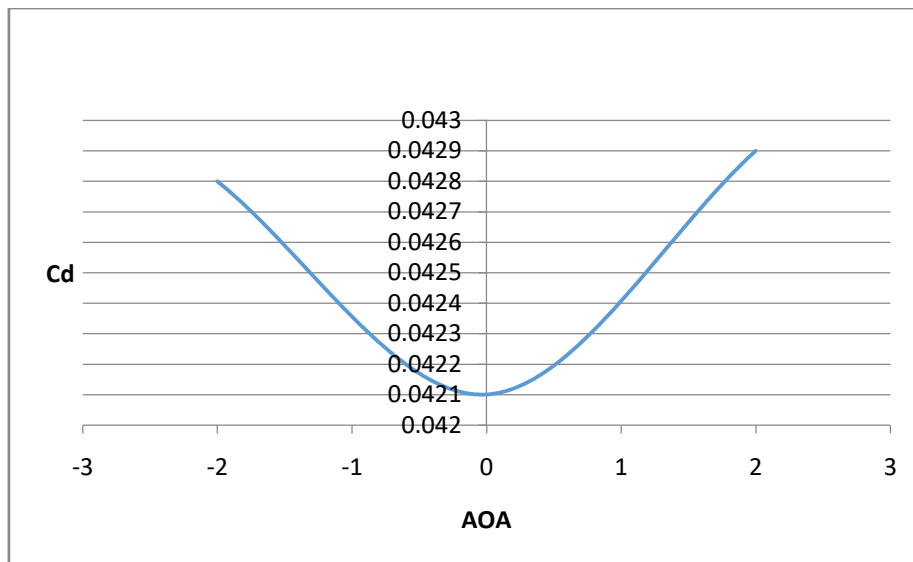


**Fig 5.3.2 Cd of Boat tail base for different AoA at 20 m/s**

The above graph shows the coefficient of drag for different angle of attack for a boat tail base configuration at 20m/s. From the graph it can be noted that the drag value increases with a change in the angle of attack, it can also be noted that at 0deg angle of attack the least value of drag is obtained.

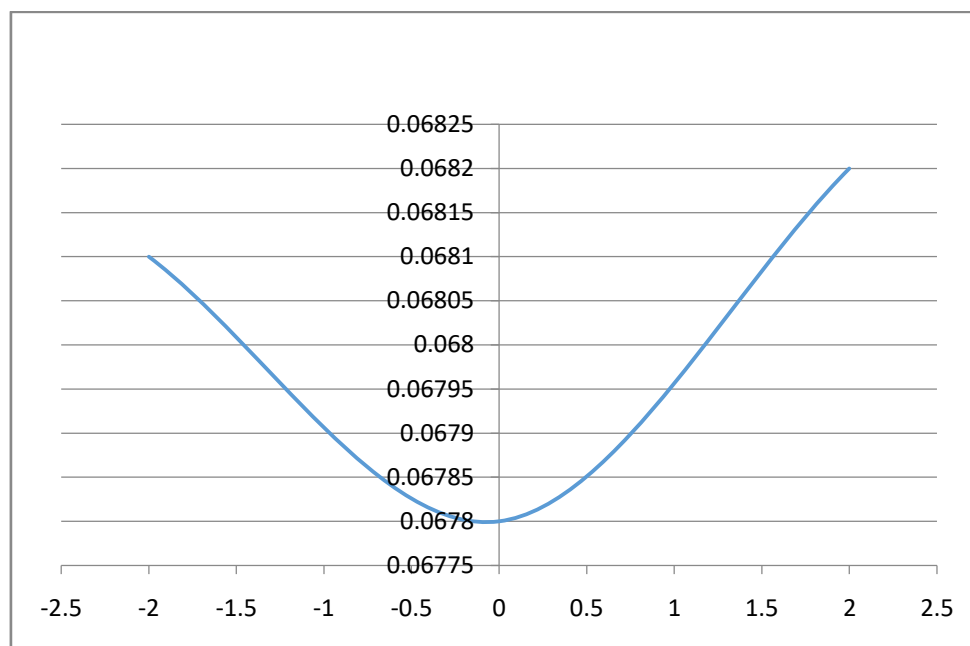


**Fig 5.3.3 Cd of nozzle base for different AoA at 20 m/s**

The above graph shows the coefficient of drag for different angle of attack for a nozzle base configuration at 20m/s. From the graph it can be noted that the drag value increases with a change in the angle of attack, it can also be noted that at 0deg angle of attack the least value of drag is obtained.

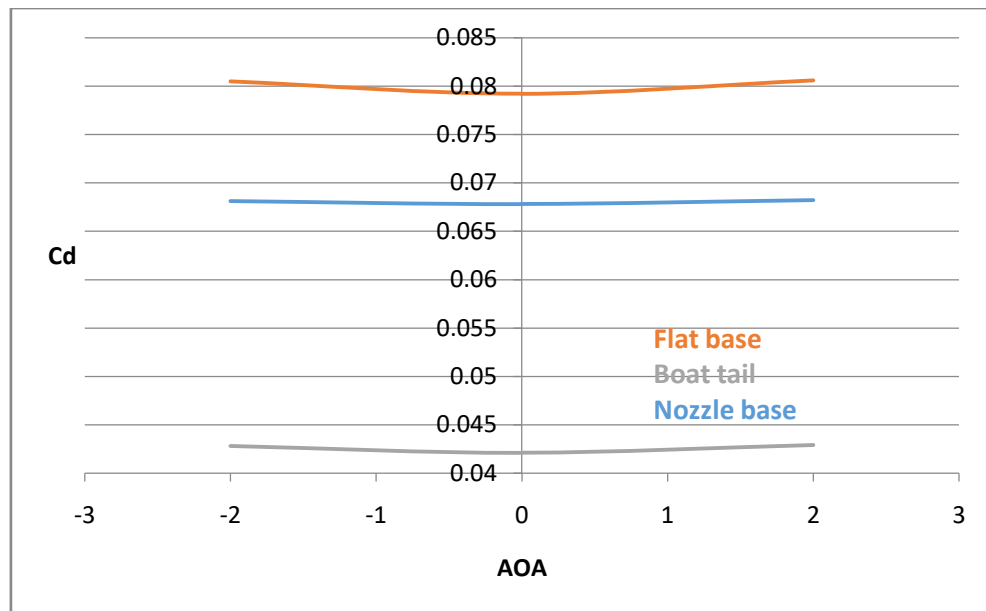


**Fig5.3.4. Comparison of  $C_d$  vs AOA for different configuration for 20 m/s**

The above graph shows the coefficient of drag comparison for all three configurations at 20m/s for different angle of attacks. From the above graph it can be clearly concluded that the boat tail base configuration gives the least amount of drag for all angle of attacks. Hence it can be concluded that boat tail configuration is the best configuration at 20m/s.

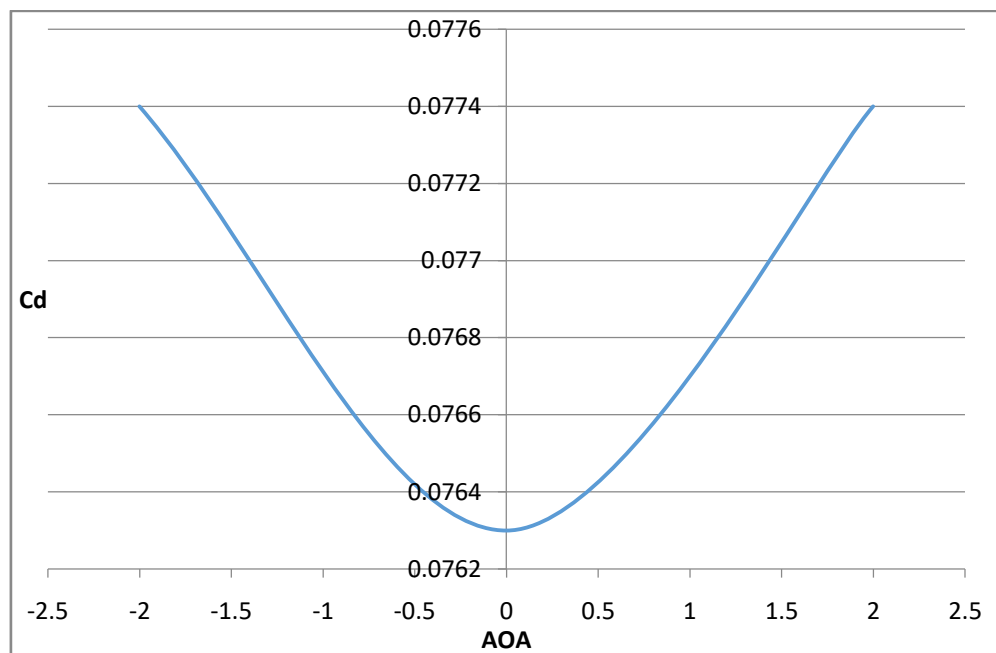


**Fig 5.3.5  $C_d$  of flat base for different AOA at 35 m/s**

The above graph shows the coefficient of drag for different angle of attack for a flat base configuration at 35m/s. From the graph it can be noted that the drag value increases with a change in the angle of attack, it can also be noted that at 0deg angle of attack the least value of drag is obtained.

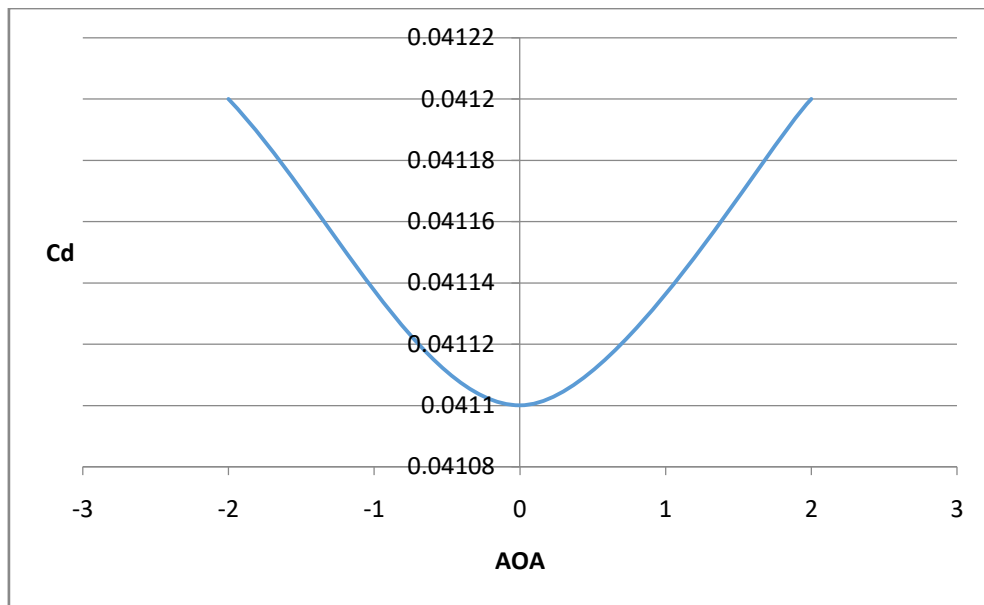


**Fig 5.3.6. Cd of boat tail base for different AoA at 35 m/s**

The above graph shows the coefficient of drag for different angle of attack for a boat tail base configuration at 35m/s. From the graph it can be noted that the drag value increases with a change in the angle of attack, it can also be noted that at 0deg angle of attack the least value of drag is obtained.

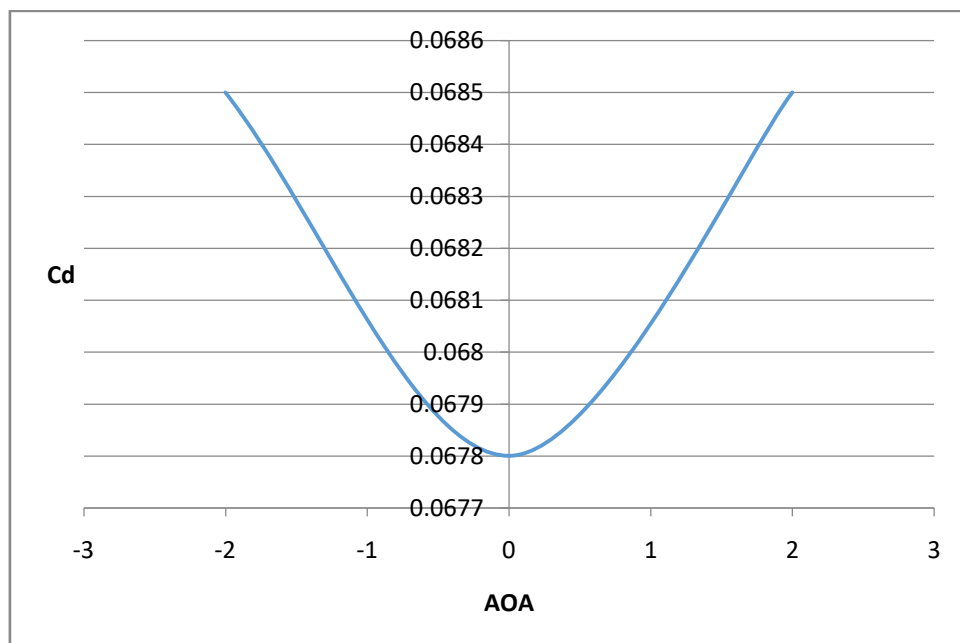


**Fig 5.3.7 Cd of nozzle base for different AoA at 35 m/s**

The above graph shows the coefficient of drag for different angle of attack for a nozzle base configuration at 35m/s. From the graph it can be noted that the drag value increases with a change in the angle of attack, it can also be noted that at 0deg angle of attack the least value of drag is obtained.

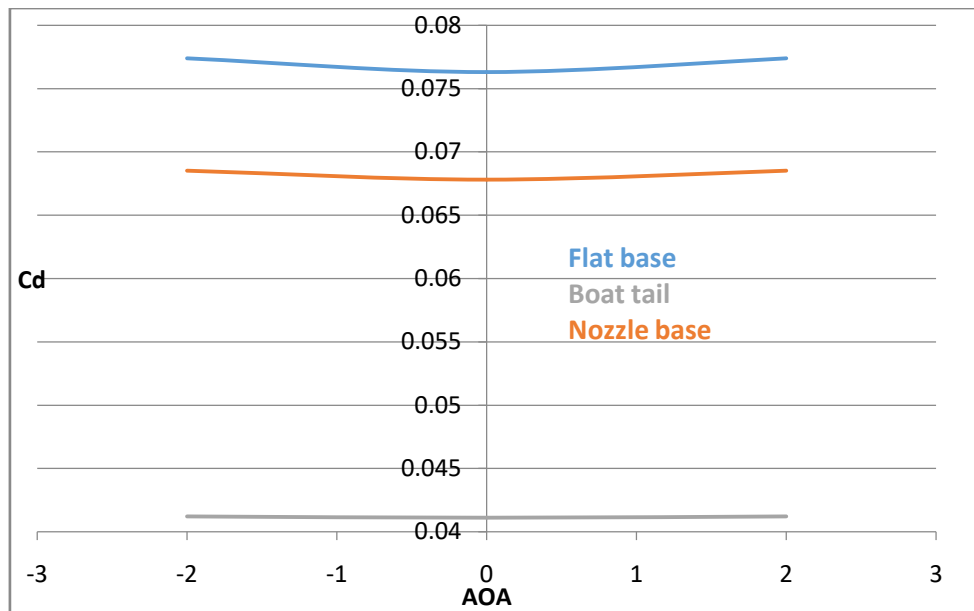


**Fig 5.3.8. Comparison of Cd vs AOA for different configuration for 35 m/s**

The above graph shows the coefficient of drag comparison for all three configurations at 35m/s for different angle of attacks. From the above graph it can be clearly concluded that the boat tail base configuration gives the least amount of drag for all angle of attacks. Hence it can be concluded that boat tail configuration is the best configuration at 35m/s.

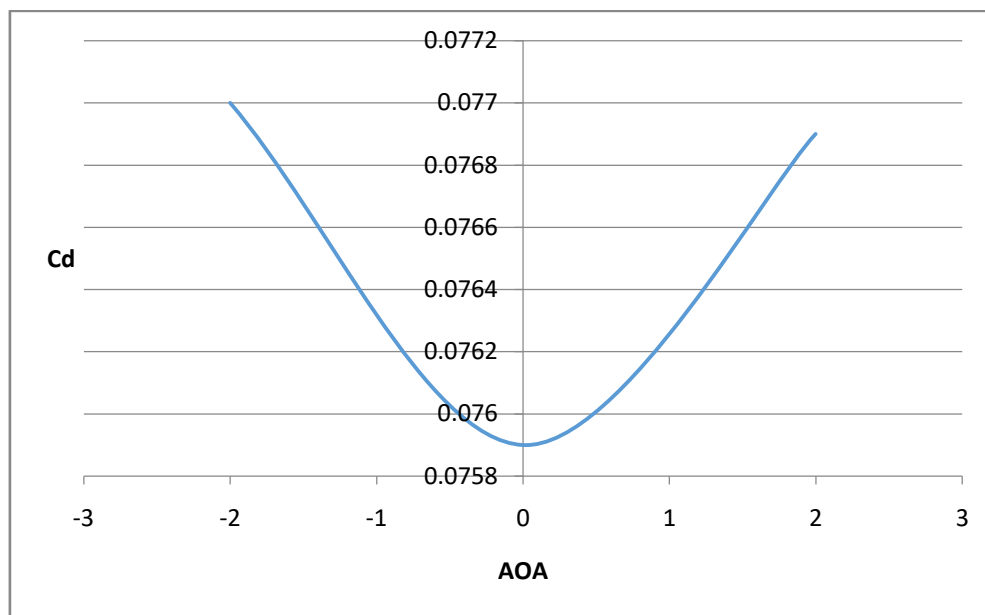


**Fig 5.3.9. Cd of flat base for different AoA at 50 m/s**

The above graph shows the coefficient of drag for different angle of attack for a flat base configuration at 50m/s. From the graph it can be noted that the drag value increases with a change in the angle of attack, it can also be noted that at 0deg angle of attack the least value of drag is obtained.

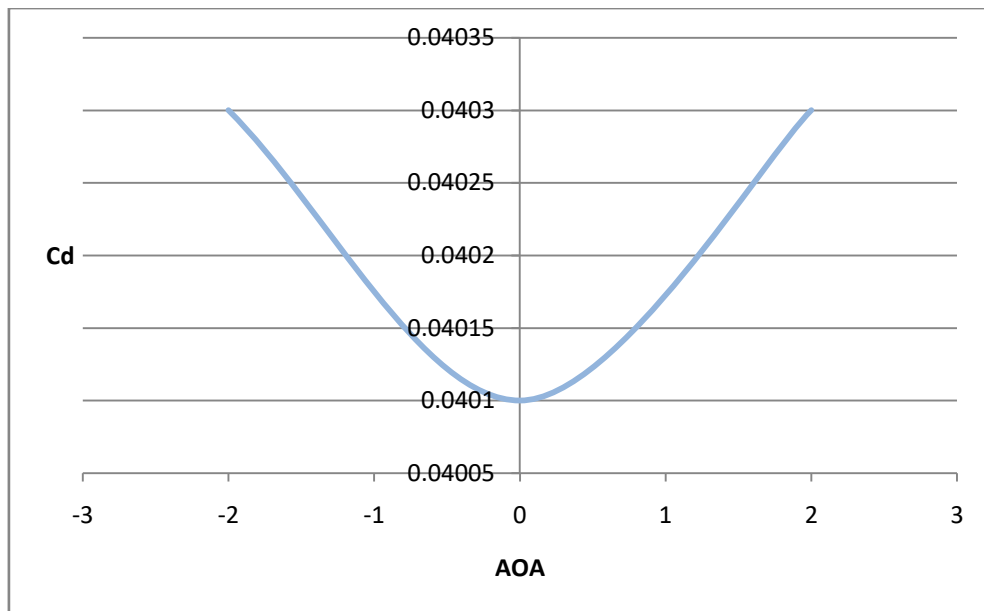


**Fig 5.3.10. Cd of boat tail base for different AoA at 50 m/s**

The above graph shows the coefficient of drag for different angle of attack for a boat tail base configuration at 50m/s. From the graph it can be noted that the drag value increases with a change in the angle of attack, it can also be noted that at 0deg angle of attack the least value of drag is obtained.

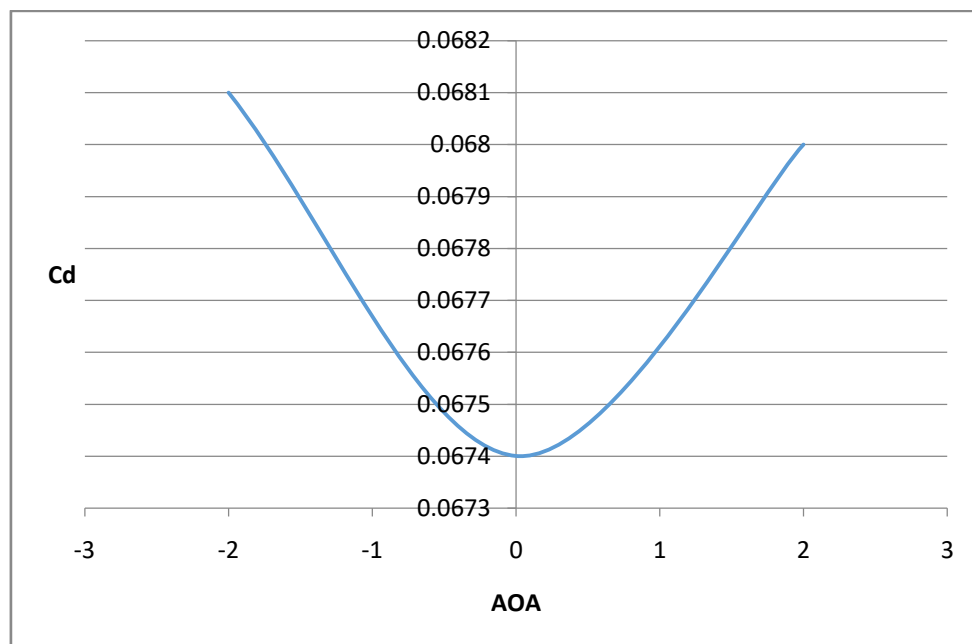


**Fig 5.3.11 Cd of nozzle base for different AoA at 50 m/s**

The above graph shows the coefficient of drag for different angle of attack for a nozzle base configuration at 50m/s. From the graph it can be noted that the drag value increases with a change in the angle of attack, it can also be noted that at 0deg angle of attack the least value of drag is obtained.



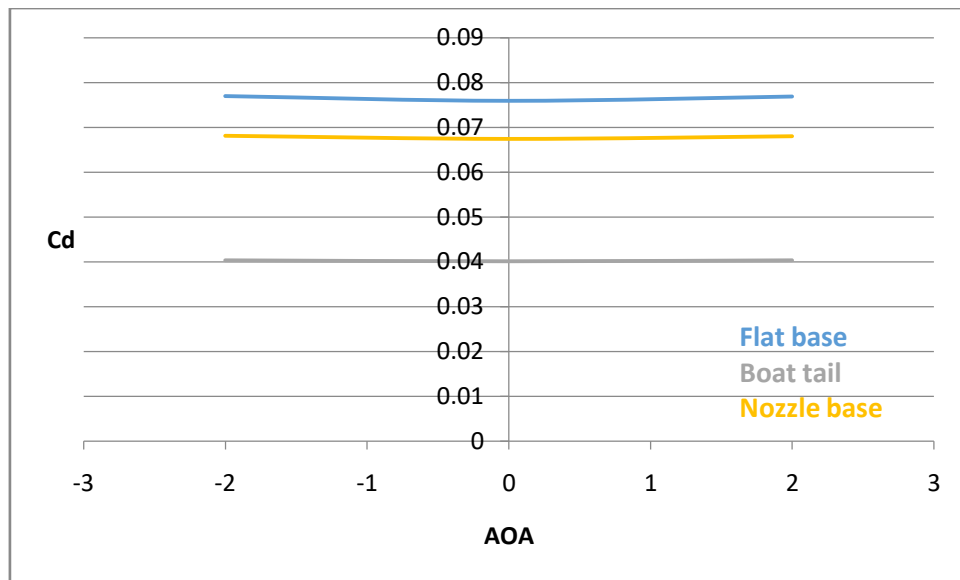


**Fig 5.3.12. Comparison of  $C_d$  vs AOA for different configuration for 50 m/s**

The above graph shows the coefficient of drag comparison for all three configurations at 50m/s for different angle of attacks. From the above graph it can be clearly concluded that the boat tail base configuration gives the least amount of drag for all angle of attacks. Hence it can be concluded that boat tail configuration is the best configuration at 50m/s.

#### 5.4. Velocity counter



**Fig 5.4.1. Velocity counter for flat base configuration at 20m/s and 0deg AOA**

The above figure shows the velocity counter for the flat base configuration at 20m/s and 0deg angle of attack. From the above figure we can make out that the velocity is maximum at the end of nose section. We can observe that the velocity after the base section is negative, this indicates that the flow is in the opposite direction i.e. flow reversal.



**Fig 5.4.2 Velocity counter for flat base configuration at 50m/s and 0deg AOA**

The above figure shows the velocity counter for the flat base configuration at 50m/s and 0deg angle of attack. From the above figure we can make out that the velocity is maximum at the end of nose section. We can observe that the velocity after the base section is negative, this indicates that the flow is in the opposite direction i.e. flow reversal.

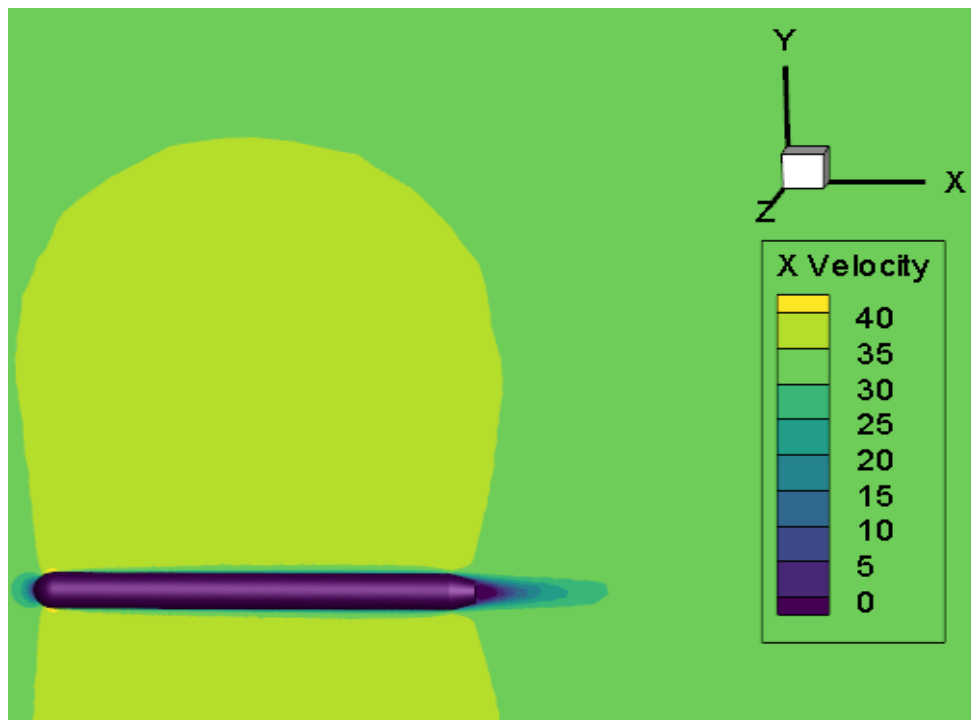


**Fig 5.4.3. Velocity counter for boat tail base configuration at 35m/s and 0deg AOA**

The above figure shows the velocity counter for the boat tail base configuration at 35m/s and 0deg angle of attack. From the above figure we can make out that the velocity is maximum at the end of nose section. We can observe that the velocity after the base section is negative, this indicates that the flow is in the opposite direction i.e. flow reversal.

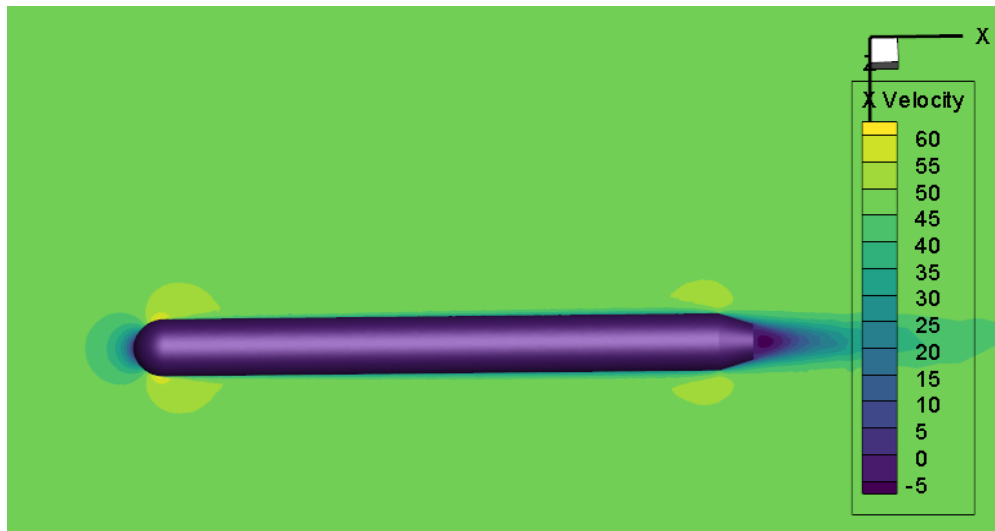


**Fig 5.4.4. Velocity counter for boat tail base configuration at 50m/s and 0deg AOA**

The above figure shows the velocity counter for the boat tail base configuration at 50m/s and 0deg angle of attack. From the above figure we can make out that the velocity is maximum at the end of nose section. We can observe that the velocity after the base section is negative, this indicates that the flow is in the opposite direction i.e. flow reversal.

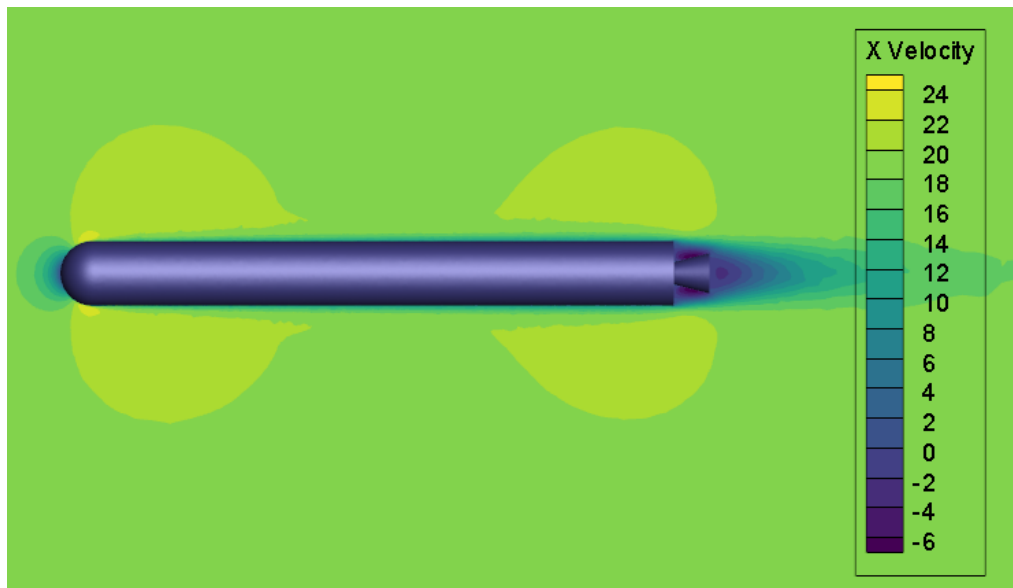


**Fig 5.4.5. Velocity counter for nozzle base configuration at 20m/s and 0deg AOA**

The above figure shows the velocity counter for the nozzle base configuration at 20m/s and 0deg angle of attack. From the above figure we can make out that the velocity is maximum at the end of nose section. We can observe that the velocity after the base section and at the beginning of the nozzle is negative, this indicates that the flow is in the opposite direction i.e. flow reversal.



**Fig 5.4.6. Velocity counter for nozzle base configuration at 35m/s and 0deg AOA**

The above figure shows the velocity counter for the nozzle base configuration at 35m/s and 0deg angle of attack. From the above figure we can make out that the velocity is maximum at the end of nose section. We can observe that the velocity after the base section and at the beginning of the nozzle is negative, this indicates that the flow is in the opposite direction i.e. flow reversal.



**Fig 5.4.7. Velocity counter for nozzle base configuration at 50m/s and 0deg AOA**

The above figure shows the velocity counter for the nozzle base configuration at 50m/s and 0deg angle of attack. From the above figure we can make out that the velocity is maximum at the end of nose section. We can observe that the velocity after the base section and at the beginning of the nozzle is negative, this indicates that the flow is in the opposite direction i.e. flow reversal.

## CONCLUSION

Base drag, being a major contributor to the total drag in the case of projectiles, can be reduced by adopting suitable techniques. One such technique being the sensible design of the missile profile by the boat tailing to reduce the drag.

A comprehensive study has been done at very low subsonic speeds using experimental techniques to study the base drag on three missile profiles by choosing the best suited experimental modeling and fabrication.

The pressure distribution on the body and the base of each missile configuration was obtained and the drag on the body due to the base pressure calculated of each of the three missile geometries. The values of the coefficient of the base drag  $C_{db}$  that were estimated were found to be higher for flat base configuration and nozzle configuration when compared to the boat tail configuration wherein we are taking only the drag at the shroud of the boat tail and the nozzle flare section. But when we consider only the base we get the base drag  $C_{db}$  higher for boat tail and flat base configuration by a small amount to that of the nozzle base. However, the  $C_{db}$  for the nozzle configuration was found to be lesser than that of baseline configuration for which the drag considerably increases with the increase in velocity and angle of attack.

From the results obtained for each of the three cases, on comparison, it was inferred that the boat tailing of the base with estimated drag at the shroud of the boat tail could be an efficient way of designing the body in order to minimize the drag of the projectile. This reduction in drag can be accounted for an increase in the range of the missile and hence prove to be much beneficial for the applications in defense purposes.

## References

1. P. Sethunathan, R. N Sugendran, T Anbarasan, Aerodynamic configuration design of missile, IJERT, Vol. 4 Issue 03, March-2015.
2. B. G. Karpov, The effect of various boattail shapes on base pressure, US Army, Ballistic Research Laboratories, Report no. 1295, August 1965.
3. Wee, Hong Chuan, Aerodynamic analysis of a missile configuration using ANSYS-CFX, Naval postgraduate school, Thesis, December 2011.
4. KwangSeop Lee, SeungKyu Hong, CFD Application and Validations in Aerodynamic Design and Analysis for missiles, USAF Academy, 3<sup>rd</sup> International symposium on integrating CFD and Experiments in Aerodynamics, 20-21 June 2007.
5. George G Brebner, General Missile Aerodynamics, AGARD LS-98, page 2-14
6. (Mitchell.et.al, Study of the Base Pressure Distribution of a Slender Body of Square Cross-Section)
7. (Hitchcock.et.al, ON ESTIMATING THE DRAG COEFFICIENT OF MISSILES)
8. (Frank G) IMPROVED EMPIRICAL MODEL FOR BASE DRAGPREDICTION ON MISSILE CONFIGURATIONS BASED ON NEW WIND TUNNEL DATA
9. (W.A.Mair.et.al) Reduction of Base Drag by Boat- Tailed After bodies in Low speed flow
10. (V.Menezes et.al.) Drag Reduction by Controlled Base Flow Separation
11. (Sidra.ISilton.et.al) Base Drag Considerations on a 0.50 caliber spinning projectile.